

UNIVERSITY OF
BIRMINGHAM

5th Annual
BEAR
PGR CONFERENCE 2014



15th December 2014

Sponsored by

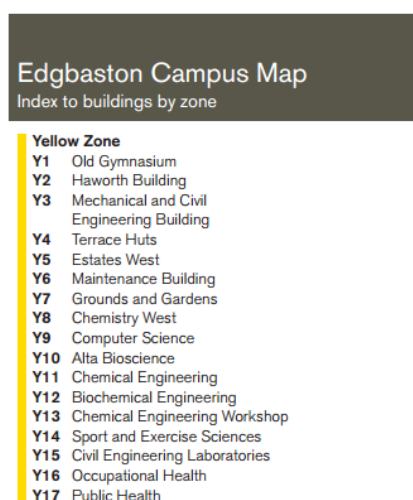
OCF



5th Annual BEAR Postgraduate Researcher Conference 2014

Welcome to the 5th annual Birmingham Environment for Academic Research (BEAR) Postgraduate Researcher Conference. The aim of this event is to provide an exciting opportunity for postgraduate students and early-career researchers to present their work to academics, industry professionals, and their peers. Keynote speakers **Adrian Gaylard from Jaguar Land Rover** and **Prof Jeffery Brooks from the School of Metallurgy and Materials** will also share their experiences of using numerical modelling in industry and academia respectively. We look forward to a day of oral and poster presentations on a wide variety of interesting research topics from across the University. There is also the chance for networking and the opportunity for discussions at the poster session at lunch, during tea and coffee breaks throughout the day, or at the conference close and prize giving ceremony.

The conference will be held in the School of Civil Engineering, University of Birmingham (Building Y3 on the campus map). Breakfast, coffee and tea, lunch, the poster session, and conference close will all take place in the Shell Lounge, with the conference presentations and keynote talks in G34 (opposite the Shell Lounge).



Organising Committee

Chris Meah (Chair)
Michaela Gkantou (Secretary)
Richard Marshall
Danique Fintelman
Fengzhen Tang
Amir Hajivayand
Zainab Al-sharify

Advisory Committee

Dr Hassan Hemida
Earl Joseph
Dr Khamis Essa
Dr Peter Hancox

Contact us: pgrsecretary@lists.bham.ac.uk

Conference Programme

Time	Speaker	Title	Chair
8:45-9:15	Registration in Shell Lounge, School of Civil Engineering (Breakfast provided)		
9:15-9:30	Prof. Richard Williams	Welcome	Dr Hassan Hemida
9:30-10:15	Adrian Gaylard	Keynote Speaker: Aerodynamics Technical Specialist, Jaguar Land Rover	
10:15-10:30	Danique Fintelman	Computational fluid dynamics study of the effect of cycling position on the aerodynamic responses in crosswinds	Chris Meah
10:30-10:45	Richard Bassett	Quantifying the influence of wind advection on the urban heat island for an improvement of a climate change adaptation planning tool	
10:45-11:00	Dr Estefania Lopez Quiroga	Operational models for ice crystal formation in highly concentrated systems	
11:00-11:30	Tea and Coffee		
11:30-11:45	Jennifer Cutter	Image-guided robotic neurosurgery through registration of 3D surface images with pre-operative CT/MRI data	Michaela Gkantou
11:45-12:00	Rachel Flight	Phase contrast image analysis for cell counting of epithelial monolayers	
12:00-12:15	Christopher Meah	Simulation of light field imaging for optimal design	
12:15-12:30	Richard Marshall	Investigating the potential for plenoptic imaging of the retina	
12:30-13:15	Lunch & Poster Viewing		
13:15-13:30	Dr Tony Price	SuSi: a monte carlo model of a novel proton CT scanner using Geant4	Richard Marshall
13:30-13:45	Jack Davis	Characterisation of chemical ordering in palladium-iridium nanoalloys	
13:45-14:00	Lewis Smeeton	Global optimisation of hydrated sulfate clusters	
14:00-14:15	Break		
14:15-14:30	Fengzhen Tang	Ordinal regression based on learning vector quantization	Danique Fintelman
14:30-14:45	Jonathan Watkins	Extrusion of a vortex lattice	
14:45-15:00	Michaela Gkantou	Numerical study of the structural response of S460 & S690 beams	
15:00-15:15	Tea and Coffee		
15:15-16:00	Prof Jeffery Brooks	Keynote Speaker: Director of PRISM2, School of Metallurgy and Materials	Dr Khamis Essa
16:00-16:15	Marjan Moalie	Effect of floodplain on the flow in asymmetric compound open channels	
16:15-16:30	Justin Morden	Effect of ballast shoulder height on a passenger trains slipstreams and wake; a computational fluid dynamics study	
16:30-16:45	Alfredo Rago	Modularity in gene expression across animal development	
16:45-17:00	Dr Hassan Hemida	Closing remarks	
17:00-17:30	Prize giving and reception (Shell Lounge)		

Posters will be on display in the Shell Lounge throughout the day. Oral presentations will be in room G34. Presenters are asked to liaise with session chairs to ensure that all presentations are uploaded in the break prior to each session. This will help keep the conference running to schedule.

Oral Presentation Abstracts & Papers

Computational fluid dynamics study of the effect of cycling position on the aerodynamic responses in crosswinds

Fintelman D.M.¹, Hemida, H.², Sterling, M. and Li, F.-X.²

¹School of Sport, Exercise and Rehabilitation Sciences, University of Birmingham, UK.

²School of Civil Engineering, University of Birmingham, UK.

dmf144@bham.ac.uk

The aim of this study was to investigate the effect of cycling position on the flow field around a cyclist and bicycle subjected to different crosswinds. Positions analysed were the 16°, 8° and 0° torso angle time trial (TT) positions, and the 24° and 16° torso angle dropped positions (DP), see Figure 1. Crosswind yaw angles varied between 0°, 15°, 30° and 45°. The flow had a velocity of 9.91 m/s. Fluid dynamic simulations were employed to determine the flow field around a cyclist and bicycle. Results showed that when lowering the torso angle within the DP or TT position, there is a significant reduction in the drag force coefficients and pitching moments. Moreover, it was demonstrated that the position (TT versus DP) primarily influences the drag forces, side forces, pitch moments and roll moments across different crosswind yaw angles. The higher drag forces in the DP at no crosswind are associated with a larger wake area and additional vortices in the leeward side of the helmet and in the wake of the arms. At large crosswind yaw angles, the TT bicycle is responsible for a significant increase in the side forces compared to the road bicycle used in the DP. It has been observed that the TT bicycle changes the underpressure at the downwind side of the bike. The results imply that in strong crosswinds, not the torso angle position but the cycling equipment plays a major role in the acting aerodynamic side forces and rolling moments, which may influence the stability of the bicycle.



Figure 1: Representation of the positioned examined in the simulations:
(a) dropped positions, (b) time trial positions

Quantifying the influence of wind advection on the urban heat island for an improvement of a climate change adaptation planning tool

Bassett R., Cai X.-M., Chapman L., Heaviside C., Thornes, J.E., Grayson N.
School of Geography, Earth and Environmental Sciences, University of Birmingham
rxb549@bham.ac.uk

Introduction

This paper presents research being conducted as part of a PhD project using numerical simulations on the BlueBEAR cluster. The project forms a partnership between the University of Birmingham and Birmingham City Council (BCC) to examine the urban heat island (UHI) and heat transport (advection) around Birmingham. The project will provide the critical evidence base to ensure that adaptation to climate change is integrated into strategic planning.

Urban heat islands are the difference in temperatures found between cities and their surrounding rural areas. The concept has been around since meteorologists such as Luke Howard (1833) identified a zone of warmer air in the city of London. The UHI can effectively be viewed as a storage heater whereby the city absorbs energy during the day and then releases it slowly at night. Physical processes responsible for the UHI include: radiation trapping due to a reduced sky view factor, changes in albedo (reflection coefficient for sunlight), a lack of vegetation, increased surface area, increased roughness, and anthropogenic heat. The magnitude or intensity of the UHI is controlled by the city size, built form (Oke, 1987), and meteorology. Clear, clam conditions at night lead to the high UHI intensities. A typical UHI profile across a city can be seen in Figure 1.

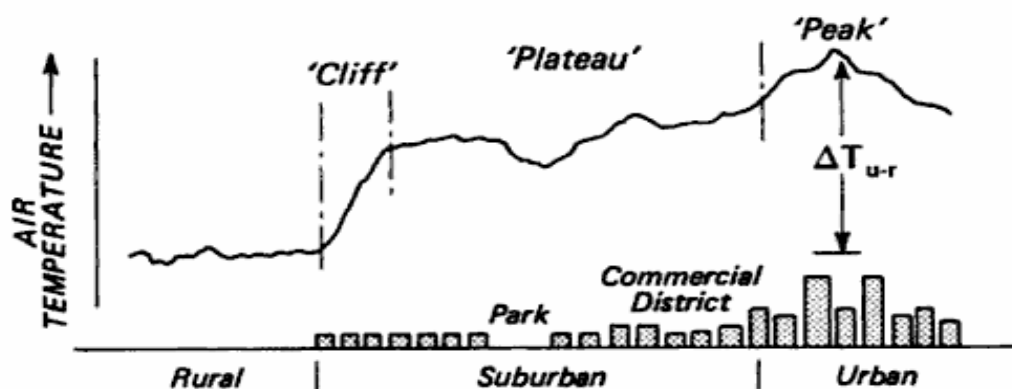


Figure 2: Typical UHI profile across a city (Oke, 1987)

UHIs in Birmingham have been shown to exceed 5°C under stable anti-cyclonic conditions (Unwin 1980). Johnson (1985) found similar readings of 4.5°C when conducting transects across the city. The spatial nature of Birmingham's UHI was outlined by Tomlinson et al. (2010) using surface temperatures derived from MODIS satellite images. Extremely stable conditions were found to produce surface UHI's up to 7°C.

A series of recent projects have examined the exact nature of the UHI in Birmingham using a variety of approaches (Tomlinson et al. 2013). The BUCCANEER (2010) (Birmingham Urban Climate Change with Neighbourhood Estimates of Environmental Risk) project used the JULES (Joint UK Land

Environment Simulator) to model Birmingham's UHI. This approach was successful in that it reproduced the UHI [Figure 2] with a good agreement with observations and showed a maximum UHI around 4°C. Whilst this is lower than observations it is important to note models have difficulty in capturing extremes. Whilst the magnitude and spatial aspect of the UHI have been well quantified, there has only recently been a notion towards the dynamic nature of the UHI in Birmingham. Wind travelling across urban areas is likely to transport heat to downwind areas. Research to date in Birmingham largely considers a static UHI, i.e. one that follows the form of the underlying land use, thus not considering the effects of wind.

There have been studies in other cities into the effect of advection on the UHI. Observationally Brandsma et al. (2003) found UHI intensity to increase by up to 1.2°C when wind blew across urban areas before reaching their rural weather station in the Netherlands. An optimal wind speed was required; too low and the advected heat would not reach the site, too high and increased turbulent mixing in the boundary layer would null the effect. Gedzelman et al. (2003) found the sea-breeze that develops off New York to displace the maximum UHI intensity up to 10km from the city centre. Unger et al. (2010) discovered 6 different spatial UHI patterns in Szeged, Hungary to be directly controlled by the wind speed and direction.

These features have also been demonstrated through modelling approaches (Liu et al. 2006; Bohnenstengel et al. 2011; Chemel and Sokhi 2012; Takane et al. 2013; Heaviside and Cai 2014). Indeed Heaviside and Cai (2014) found a 2.5°C temperature difference between modelled upwind and downwind temperatures in Birmingham for the 2003 heatwave period.

In order to model advection a suitable model that contains both dynamic (wind) effects and an urban land surface scheme is required. For this study the mesoscale Weather Research & Forecasting (WRF) model is chosen. WRF is a community based (25,000 users worldwide) nonhydrostatic mesoscale model. The model has been demonstrated to be capable of reproducing urban climate in many global cities in addition to being suitable for a variety of applications ranging from regional climate to hurricanes. The modelling system computes physical processes such as radiative transfer, clouds, precipitation, turbulence, wind and surface fluxes (heat, moisture and momentum). The number of processes WRF computes means it can be computationally demanding.

The interaction between the Earth's surface and atmosphere is controlled by the surface energy balance ($Q^* = Q_H + Q_E + Q_G$) or the partitioning of energy from net all wave radiation (Q^*) into sensible (Q_H) and latent (Q_E) heat fluxes, and conduction into the ground (Q_G). Urban areas rework this balance ($Q^* + Q_F = Q_H + Q_E + \Delta Q_S + \Delta Q_A$) to add anthropogenic heat (ΔQ_F), storage (ΔQ_S) and advected heat (ΔQ_A). Solving this modified energy balance is the basis for modelling urban areas. It must be noted however that this is only a small component of what is required to model UHIs. Due to the inherent complexities parameterisations must be made.

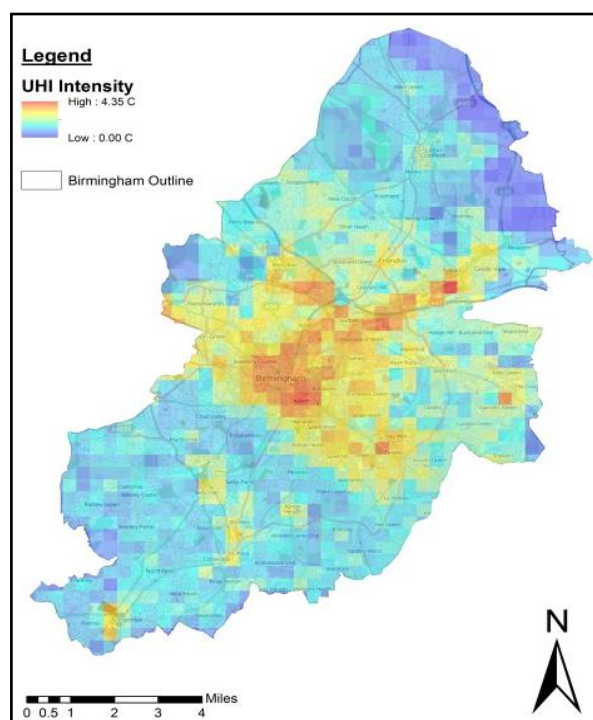


Figure 3: UHI in Birmingham using the JULES model

A series of these parameterisations or urban canopy schemes have been coupled to WRF in order to capture the impacts of urbanisation on near-surface meteorology. These range from a basic SLAB scheme (Liu et al. 2006) that mimics urban areas through modifying surface variables such as the albedo to BEP (Building Effect Parameterisation, Martilli et al. 2002) which consists of canyons that protrude into the atmosphere. BEP enables a separate surface energy balance to be calculated for the three surfaces, roads, walls and roofs within the canyon. BEP is able to provide a more realistic thermal representation of urban areas vertically than the simpler models and also account for the building effects on momentum. A review of the urban schemes used in WRF can be found in Chen et al. 2011. For this study we choose to use the WRF-BEP modelling framework due to its ability to capture process at different levels throughout the atmospheric boundary layer

WRF modelling using BlueBEAR

A high resolution run using the WRF version 3.6 is conducted on the BlueBEAR cluster. The model is set up with 4 nested domains of increasing resolution (36km, 12km, 3km and 1km) covering the West Midlands in the smallest domain (Figure 3). Nests are used to reduce computational time. A local land use map combining local urban categories specific to the West Midlands (Owen et al. 2006) was re-categorised to three urban categories that BEP uses: (1) Commercial/Industrial/Transportation (2) High intensity residential (3) Low intensity residential. Default model physics and BEP parameters are currently used. Two-way nesting is permitted. These parameters will be fine-tuned specifically for Birmingham during the project.

Domain	01	02	03	04
Resolution	36km	12km	3km	1km
Grid cells (Horizontal x Vertical)	50x41	52x29	69x65	82x79

European Centre for Medium-Range Weather Forecasts (ECMWF) ERA-40 interim (Uppala et al. 2005) initial and lateral boundary conditions are used to drive the model. This is a 40-year global atmospheric reanalysis (i.e. historic values) of the state of the atmosphere. The product is estimated from computer analysis of atmospheric conditions taken from past observations and satellite data. It provides 6-hourly atmospheric and surface fields at a spatial resolution of 125km. Fields include wind, temperature and water vapour. The model is run for an 8-day period (12th -20th July 2013) using the BlueBEAR cluster. This period is chosen due to being exceptionally warm and was

characterised by the Met Office as a heatwave. The period of hot, dry weather extended from the 3rd to 23rd July 2013, where daily maximum temperatures exceeded 28°C every day somewhere in the UK. Simulations take approximately 7 hours using 32 processors. Total CPU time for the run is approximately 225 hours. An example of the model output can be seen in Figure 4.

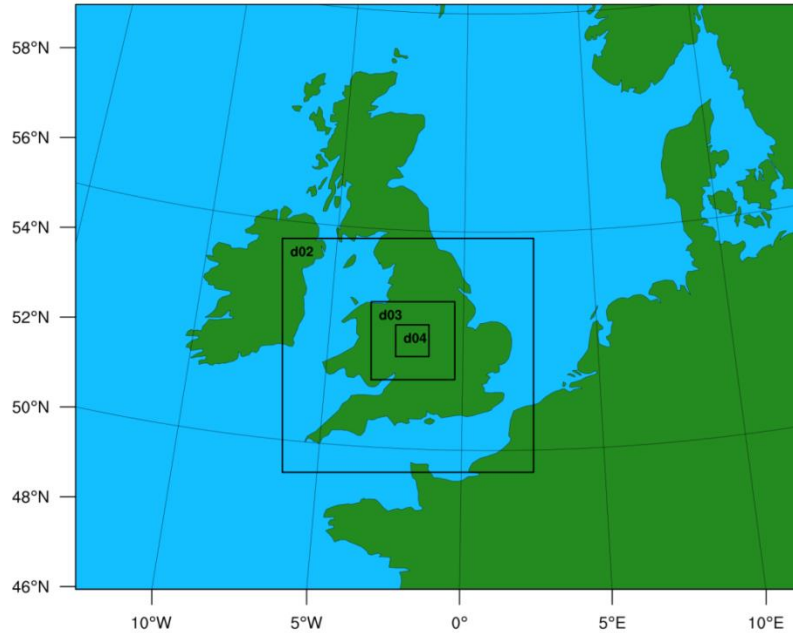


Figure 4: WRF domains and resolution

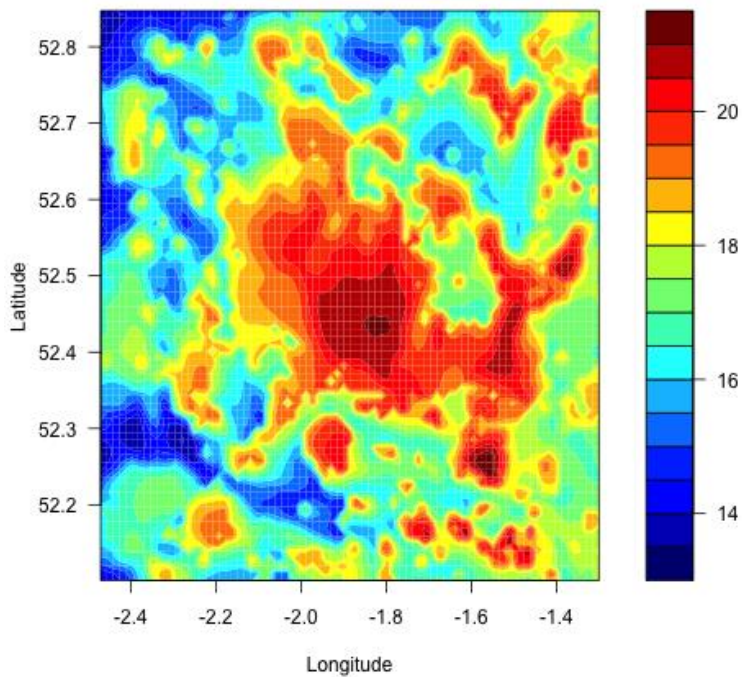


Figure 5: WRF domain 4 Temperature (°C) at 2 m 15th July 00:00AM.

Across Birmingham there are four Met Office weather stations: Winterbourne (University of Birmingham), Paradise Circus (City Centre), Coleshill (rural) and Elmdon (airport). In conjunction with these sites is a network of automatic weather stations (Vaisala WXT) from the multi-scale urban climate dataset HiTemp. These stations show a reasonable agreement with the modelled results, however some differences are noted. A RMSE (Root Mean Square Error) for urban simulations at Paradise Circus (Figure 5) of 1.3°C is found and suggests the urban component of the model is performing well. However the WRF model seems to under predict daytime rural temperatures and does not cool down as much as the observations. Initial investigations suggest this could be due to specified soil moisture content and incorrect land use specification. The default WRF USGS rural land use configuration assumes the UK to be largely dryland crops when in reality it is a mosaic of different categories.

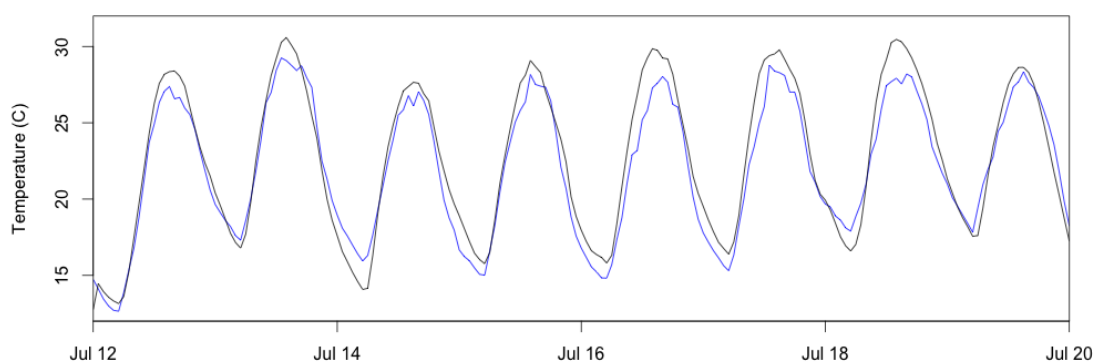


Figure 6: WRF (black) compared with observed (blue) temperatures at the city centre site, Paradise Circus

Project Directions

This initial simulation shows the WRF model is able to capture urban temperatures. However fine-tuning specifically for Birmingham is still required. A series of sensitivity tests will also be conducted on BlueBEAR changing initial conditions such as the soil moisture and model parameters. The next stages of the analysis will investigate advection effects across Birmingham using a similar methodology to Heaviside and Cai [2014] who decomposed the UHI intensity at a given location into what is created by local mechanisms (land use, topography) and what is advected. Furthermore idealised simulations will be run to further determine the advected heat contribution when the complex nature of an urban area is simplified.

Once wind advection is quantified using WRF, a generic methodology of correcting UHI patterns (i.e. JULES simulation in Figure 1) from local-equilibrium models (no grid cell transport of heat and momentum) can be developed. This will be incorporated through a spatial-lag correlation of the wind advection affect. This methodology will be beneficial to land surface model development.

The project will also develop impact through an on-going partnership with Birmingham City Council to deliver improvement of an existing risk mapping tool that was originally developed through the BUCCANEER project. The tool includes UHI, climate and social-environment data displayed through visual mapping to conduct a spatial risk assessment that will feed into policy development at the council

References

- Bohnenstengel SI, Evans S, Clark PA, Belcher SE. 2011. Simulations of the London urban heat island. *Q. J. Roy. Meteor. Soc.* 137(659): 1625 - 1640.
- Brandsma T., Konnen GP., Wessels HRA., 2003. Empirical estimation of the effect of urban heat advection on the temperature series of De Bilt (The Netherlands). *Int. J. Climatol.* 23, 829–845.
- Chemel C, Sokhi RS. 2012. Response of London's Urban Heat Island to a Marine Air Intrusion in an Easterly Wind Regime. *Boundary-Layer Meteorol.* 144 65-81.
- Chen, F. and Dudhia, J. (2001) Coupling an advanced land surface-hydrology model with the Penn State-NCAR MM5 modeling system. Part I: Model implementation and sensitivity. *Monthly Weather Review*, 129: (4): 569-585.
- Chen, F., Kusaka, H., Bornstein, R., et al. (2011) The integrated WRF/urban modelling system: development, evaluation, and applications to urban environmental problems. *International Journal of Climatology*, 31: (2): 273-288.
- Gedzelman, S., Austin, S., Cermak, R., 2003. Mesoscale aspects of the urban heat island around New York City. *Theor. Appl. Climatol.* 42, 29–42.
- Heaviside C, Cai X-M, Vardoulakis S. 2014 The effects of horizontal advection on the urban heat island in Birmingham and the West Midlands, United Kingdom during a heatwave. *Q. J. R. Meteorol. Soc. HiTemp. High Density Measurements within the Urban Environment* <http://goo.gl/CMha6h>
- Howard L. 1833. *The Climate of London*
- Johnson D. 1985. Urban modification of diurnal temperature cycles in Birmingham, U.K. *Int. J. Climatol.* 5: 221–225.
- Liu, Y., Chen, F., Warner, T., Basara, J., 2006. Verification of a Mesoscale Data-Assimilation and Forecasting System for the Oklahoma City Area during the Joint Urban 2003 Field Project. *J. Appl. Meteorol. Climatol.* 45, 912–929.
- Martilli A, Clappier A, Rotach MW. 2002. An urban surface exchange parameterisation for mesoscale models. *Boundary-Layer Meteorology* 104: 261–304.
- Met Office. Hot dry spell July 2013. <http://www.metoffice.gov.uk/climate/uk/interesting/2013-heatwave>. Accessed 12/11/2014.
- Oke TR. 1987. *Boundary Layer Climates*. Methuen: London.
- Owen S, MacKenzie A, Bunce R, Stewart H, Donovan R, Stark G, Hewitt C. 2006. Urban land classification and its uncertainties using principal component and cluster analyses: A case study for the UK West Midlands. *Landscape and Urban Planning* 78: 311–321
- Takane, Y., Ohashi, Y., Kusaka, H., Shigeta, Y., Kikegawa, Y., 2013. Effects of Synoptic-Scale Wind under the Typical Summer Pressure Pattern on the Mesoscale High-Temperature Events in the Osaka and Kyoto Urban Areas by the WRF Model. *J. Appl. Meteorol. Climatol.* 52, 1764–1778.
- Tomlinson CJ, Chapman L, Thornes JE, Baker CJ. 2012. Derivation of Birmingham's summer surface urban heat island from MODIS satellite images. *Int. J. Climatol.* 32: 214–224.
- Tomlinson CJ, Priteo-Lopez T, Bassett R, Chapman L, Cai X-M, Thornes JE, Baker CJ. 2013. *Showcasing urban heat island work in Birmingham – measuring, monitoring, modeling and more. Weather.* 68: 44-49.
- Unger, J., Sümeghy, Z., Szegedi, S., Kiss, A., Géczy, R., 2010. Comparison and generalisation of spatial patterns of the urban heat island based on normalized values. *Phys. Chem. Earth, Parts A/B/C* 35, 107–114.
- Unwin DJ. 1980. The synoptic climatology of Birmingham's urban heat island, 1965-74. *Weather* 35: 43–50.
- Uppala, S.M., Kållberg, P.W., Simmons, A.J., Andrae, U., da Costa Bechtold, V., Fiorino, M., Gibson, J.K., Haseler, J., Hernandez, A., Kelly, G.A., Li, X., Onogi, K., Saarinen, S., Sokka, N., Allan, R.P., Andersson, E., Arpe, K., Balmaseda, M.A., Beljaars, A.C.M., van de Berg, L., Bidlot, J., Bormann, N., Caires, S., Chevallier, F., Dethof, A., Dragosavac, M., Fisher, M., Fuentes, M., Hagemann, S., Hólm, E., Hoskins, B.J., Isaksen, I., Janssen, P.A.E.M., Jenne, R., McNally, A.P., Mahfouf, J.-F., Morcrette, J.-J., Rayner, N.A., Saunders, R.W., Simon, P., Sterl, A., Trenberth, K.E., Untch, A., Vasiljevic, D., Viterbo, P., and Woollen, J. 2005: The ERA-40 re-analysis. *Quart. J. R. Meteorol. Soc.*, 131, 2961-3012.

Operational models for ice crystal formation in highly concentrated systems

E. López-Quiroga, P.J. Fryer, O. Gouseti, R. Wang and S. Bakalis

School of Chemical Engineering, University of Birmingham, UK.

e.lopez-quiroga@bham.ac.uk

Abstract

Freezing is one of the most employed procedures in food manufacturing and preservation, determining the quality and safety of the final frozen product, as well as the performance in further operations, often controlled by mean size and distribution of the crystals formed during the process. In this work, two spatially distributed models based on first-principles are presented to provide a description of the freezing dynamics and the related ice crystal formation. These multi-scale models are intended to help in the understanding of the phenomena and also in the design of targeted product microstructure. A system consisting of a sucrose solution 60% by weight has been chosen as case study in order to demonstrate the advantages of this modelling-based approach.

Introduction

Controlling ice crystal formation is critical in determining the microstructure and quality of frozen foods in processes such as freezing and freeze-drying [1]. As recent trends in food processing head towards the manufacturing of highly concentrated foodstuff, efficient performance of such industrially relevant crystallisation processes has become increasingly difficult. The upcoming challenges therefore rely not only in developing successful processing protocols but also in the understanding the insights of these systems. In this framework, mathematical modelling can be employed to obtain an accurate description of the system behaviour as well as to help in the comprehension of the process dynamics [2]. As such, operational models have emerged as useful tools in the design and optimisation of food industry protocols. Typically, freezing processes are simulated by following one the following approaches: front-tracking methods, apparent/equivalent specific heat methods or by coupling the expression of the global crystallisation kinetics to the general heat transfer problem [3,4]. However, the modelling of freezing and crystallisation phenomena in high concentrated systems is not well addressed yet in food processing literature, as inferred from a recent review [5]. In this framework, the present contribution presents two freezing models based on first principles, which aim at helping in the study and analysis of the different crystallisation processes that can occur during the freezing of sucrose solutions with a high content in solids (60% w/w). Effects of including air in the product formulation are further studied.

Experimental procedure

Sucrose was mixed (magnetic stirrer) with distiller water under heating (max 50°C) in closed container to prepare a solution of concentration 60% by weight. Solutions were left to cool at room temperature and used within 24h. Differential scanning calorimeter (DSC) experiments have been conducted in order to characterise the crystallisation kinetics of water during freezing. In addition, a series of seeding experiments (secondary nucleation) in a 60% w/w sucrose solution have been performed too, and images of the growth process were recorded at suitable time intervals for data treatment.

Mathematical models

Two different models for the description of the freezing process have been developed. The first model aims at representing the seeding experiments (secondary nucleation) referred to in Section 2.3. It makes use of the classical formulation of Stefan problems [4], which considers the material undergoing the phase change is divided into two subdomains (one for each water thermodynamic state) separated by the moving phase change front. By assuming an initially small frozen domain (the seed), secondary ice crystal formation can be simulated. A front-tracking method based on an ALE algorithm [6] for adaptive grids has been employed in the numerical treatment of the moving front in this case. For the numerical simulation of the homogeneous crystallisation mechanism, heat transfer has been coupled to ice crystal nucleation and growth kinetics. A heat source term accounting for the energy of the phase change has been included in the formulation of the problem. In addition, aeration effects will be also taken into account for this second freezing scenario.

Secondary nucleation: seeding modelling

Ice crystal growth from a pre-existing nuclei (i.e. seed) can be described by considering the following heat and mass coupled PDE system formulated in a 1D axisymmetric radial domain, as the one depicted in Figure 1:

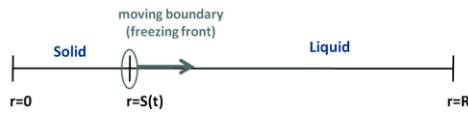


Figure 1: Spatial domain considered in the modelling of the secondary nucleation phenomenon.

$$\frac{\partial c_i}{\partial t} = \nabla(D_i \nabla c_i), \quad i = l, s \quad (1)$$

$$\rho_i C_{p_i} \frac{\partial T_i}{\partial t} = \nabla(k_i \nabla T_i), \quad i = l, s \quad (2)$$

$$\left[c \Big|_{S(t)^+} - c \Big|_{S(t)^-} \right] \frac{\partial S}{\partial t} = D_l \frac{\partial c}{\partial x} \Big|_{S(t)^+} - D_s \frac{\partial c}{\partial x} \Big|_{S(t)^-} \quad (3)$$

$$\Delta H \rho_s \frac{\partial S}{\partial t} = -k_l \frac{\partial T}{\partial x} \Big|_{S(t)^+} + k_s \frac{\partial T}{\partial x} \Big|_{S(t)^-}; T_i(S(t), t) = T_f^* - \Delta T \quad (4)$$

$$T_s(0, t) = T_c < T_i(S(t), t); \frac{\partial T_l}{\partial r}(R, t) = 0 \quad (5)$$

$$c_s(0, t) = c_{seed}; \frac{\partial c_l}{\partial r}(R, t) = 0 \quad (6)$$

where c_i (w/w) and T_i ($^{\circ}\text{C}$) read for concentration and temperature, respectively, of the liquid (l) and solid (s) fractions. The density, heat capacity and heat conductivity, are denoted by ρ_i (kg/m^3), C_{p_i} (J/kgK) and k_i (W/mK), being D_i (m^2/s) the mass diffusivity, ΔH (J/kg) the phase change enthalpy and T_f^* ($^{\circ}\text{C}$) the freezing temperature of pure water. The freezing-point depression, ΔT , for sucrose solutions is described as in [7].

Primary homogeneous crystallisation

In the modelling of homogeneous crystallisation, heat transfer phenomenon has been coupled to both nucleation and growth crystal kinetics [3]:

$$\rho_m C_{p_m} \frac{\partial T_m}{\partial t} = \nabla(k_m \nabla T_m) + \rho_s \Delta H \frac{\partial \alpha}{\partial t}; \quad T_s(0, t) = T_c < T_i(S(t), t); \frac{\partial T_l}{\partial r}(L, t) = 0 \quad (7)$$

where α represents the fraction of ice crystals, which has been computed by employing the DSC based method presented in [8], and L (m) is the length of the sample.

$$\begin{aligned}
 k_m &= \varepsilon k_{air} + (1-\varepsilon)(\alpha k_s + [1-\alpha]k_l) \\
 C_{p_m} &= \varepsilon C_{p_{air}} + (1-\varepsilon)(\alpha C_{p_s} + [1-\alpha]C_{p_l}) \\
 \rho_m &= \varepsilon \rho_{air} + (1-\varepsilon)(\alpha \rho_s + [1-\alpha]\rho_l)
 \end{aligned} \quad (8)$$

The thermophysical properties of the solution have been defined by employing a mixing rule between liquid and solid phases values weighted by the crystalline fraction α . The effects of including air in the system have also been studied for this scenario. The air volume fraction ε has been also considered in the definition of the product properties, as it reads in equation(8).

Results and Discussion

Model validation

In order to verify the validity of the modelling approaches presented in Section 3, numerical simulations have been performed by employing data and parameters corresponding to pure water. This scenario of validation reduces the seeding model presented in Section 3.1 to the thermal problem formed by equations (2) and (4), together with the external boundary conditions for temperature defined by equation (5). It must also be mentioned that for the homogeneous process, the front position has been obtained in a post-processing step by means of the crystal fraction $\alpha(T)$, which has been defined as Heaviside step function with a transition interval $\delta T = 0.1$ around $T_f^* = 0$ °C. Both models have been implemented and solved in a commercial FEM software (COMSOL Multiphysics), making use of a spatial grid with $N=101$ nodes, and the PARDISO solver, with tolerances equal to $tol = 10^{-6}$. For the seeding model, the FEM has been combined with an ALE algorithm in order to adapt the mesh to the front advance. On the contrary, a fixed grid implementation has been employed for the solution of the homogeneous ice crystal formation model. Results regarding the freezing front advance throughout the considered sample ($L=0.01$ m) are shown in Figure 2, and show good agreement with those provided by the analytical solution of the thermal problem [3].

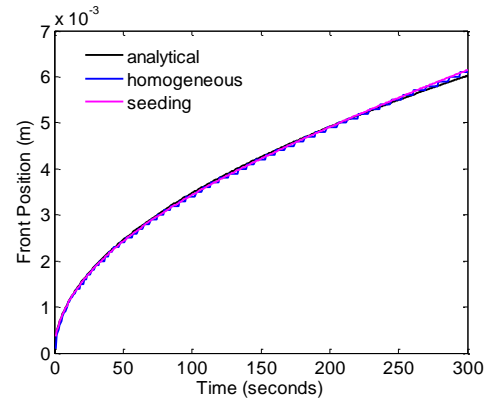


Figure 2: Comparison of the freezing front position evolution in time between the analytical and the proposed models solutions.

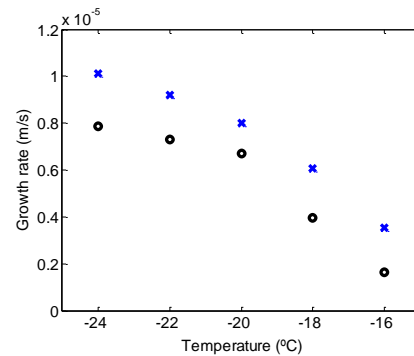


Figure 3: Comparison of experimental (o) and simulated (x) growth crystal rates for different cooling conditions.

Results from seeding modelling

The freezing model presented in Section 3.1 for secondary nucleation has been solved by employing the numerical procedure explained in Section 4.1. As shown in Figure 3, realistic values for crystal growth rates have been computed from numerical simulation results, which are overall in good agreement with experimental observations albeit systematically higher. It must be noted that these

simulation results have been obtained under the assumption of thermodynamic equilibrium at the phase change front, while experimental data have been recorded in a system presumably under non-equilibrium and with non perfect Neumann conditions.

Results of the primary homogeneous crystallisation modelling

The system formed by equations (7) and (8) has been solved for a 60% w/w sucrose solution and different air fractions: $\varepsilon = [0.1, 0.2, 0.3]$ by following the method aforementioned in Section 4.2. It has been found that the addition of air tends to delay the crystal formation, as can be seen in Figure 4. This is understood as a direct consequence of the insulating effect of air within the product, which slows down the heat transfer through the sample [1].

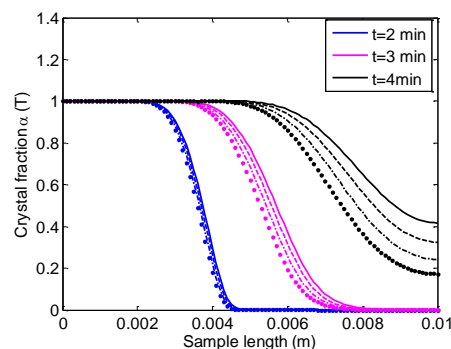


Figure 4: Comparison of the crystal fraction $\alpha(T)$ along the sample between the non-aerated 60 % w/w sucrose solution (solid), and the aerated solution with air fractions $\varepsilon = 0.1$ (dashed), $\varepsilon = 0.2$ (dashed-dot) and $\varepsilon = 0.3$ (dot).

Conclusions

A first approach to the modelling of crystallisation phenomena (both primary and secondary mechanisms) in highly concentrated systems has been presented. This constitutes an important contribution towards the design of targeted frozen product microstructure, which is a key factor not only for the quality of frozen foods but also in other freeze-related processes such as freeze concentration and freeze drying [5,9].

Acknowledgements

The authors acknowledge financial support received from EPSRC (grant no. EP/K011820/1).

References

- [1] Petzold, G. and Aguilera, J.M. 2009. Ice morphology: fundamentals and technological applications in foods. *Food Biophysics* 4, 378-396.
- [2] Cameron, I. and Hangos, K. (2001). *Process modelling and model analysis*. Academic Press, London.
- [3] Chégnimonhan, V., Josset, C. and Peerhossaini. 2010. Ice slurry crystallization based on kinetic phase-change modeling. *International Journal of Refrigeration* 33, 1559-1568.
- [4] Crank J. 1984. *Free and moving boundary problems*, Clarendon Press, Oxford, UK.
- [5] Sánchez, J., Ruiz, Y., Auleda, J. M., Hernández, E., and Raventós, M. 2009. Review. Freeze concentration in the fruit juices industry. *Food Science and Technology International*, 15, 303-315.
- [6] Donea, J., Huerta, A., Ponthot, J-P. and Rodríguez-Ferrán, A. 2004. *Encyclopedia of Computational Mechanics*, Volume I, Chapter 14. Wiley & Sons, Oxford, UK.
- [7] Roos, Y.H. 1995. *Phase transitions in foods*. Academic Press, London.
- [8] Málek, J. 2000. Kinetic analysis of crystallization processes in amorphous materials. *Thermochimica Acta* 335, 239-253.
- [9] Aguilera, J.M. 2005. Why food microstructure? *Journal of Food Engineering*, 67, 3-11.

Image-Guided Robotic Neurosurgery through Registration of 3D Surface Images with Pre-operative CT/MRI Data

Jennifer R. Cutter^{1,2}, Aleš Leonardis², Hamid Dehghani^{1,2} and Iain B. Styles^{1,2}

¹School of Computer Science, University of Birmingham, UK.

²PSIBS Doctoral Training Centre, University of Birmingham, UK.

jrc133@bham.ac.uk

Stereotactic neurosurgical robots are used to reach and perform surgery on small targets within the brain. Targets are located on preoperative images and the robot end effector is moved to the coordinates specified: this requires the robot's coordinate system to be accurately registered with the patient's, and the preoperative images. Registration is performed using either a stereotactic frame or fiducial markers as landmarks. During surgery the patient's head is kept fixed in position.

The aim of this work is to co-register optical images of a patient's head surgery during with preoperative CT/MRI

images, allowing the head's location to be changed and its new coordinate system to be registered with the robot and giving greater ease of access to the head, while retaining the required surgical precision.

3D point cloud representations of a phantom head were obtained using a 3D surface capture system developed by Basevi et al, 2013 [1] and a Microsoft

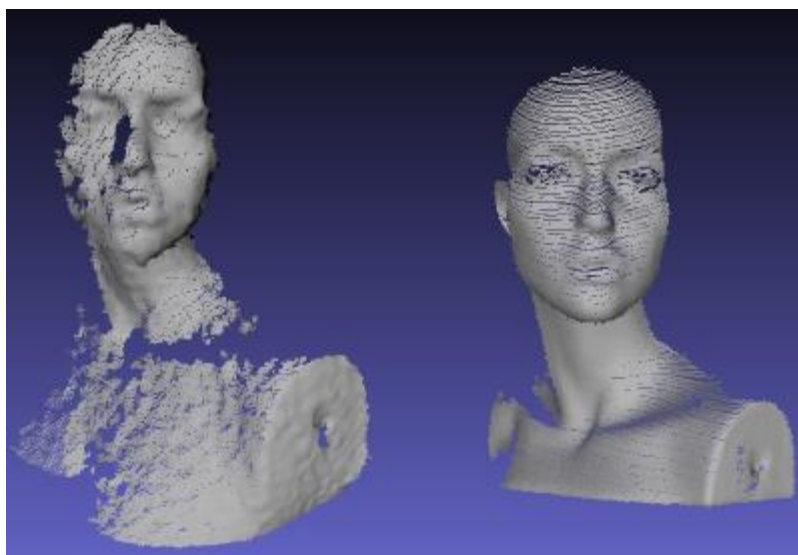


Figure 7: Kinect (left) and surface capture point clouds of a mannequin head.

Kinect for Windows sensor (Figure 1).

The point clouds were registered with the ground truth for the phantom using the iterative closest point algorithm (ICP); different versions of ICP were compared. The point clouds taken using the surface capture system were a closer match to the ground truth than those from the Kinect sensor. 3D normal distribution transforms (3D-NDTs) were created for the point clouds using various methods in order to perform 3D-NDT registration using the method described in Magnusson, 2009 [2].

References

[1] Basevi, H. R., Guggenheim, J. A., Dehghani, H., & Styles, I. B. 2013. Simultaneous multiple view high resolution surface geometry acquisition using structured light and mirrors. *Optics express*, **21**(6), 7222-7239.

[2] Magnusson, M. 2009. *The three-dimensional normal-distributions transform: an efficient representation for registration, surface analysis, and loop detection*. Örebro universitet.

Phase contrast image analysis for cell counting of epithelial monolayers

R. Flight¹, G. Landini², I. Styles³, M. Milward², R. Shelton² and P. Cooper²

¹PSIBS DTC, University of Birmingham, UK.

²School of Dentistry and ³School of Computer Science, University of Birmingham, UK

rx144@bham.ac.uk

Manual cell counting using a haemocytometer is a destructive method thus several cultures must be maintained simultaneously to generate growth curves, which requires both time and resources. The method is also subject to high operator variability. Phase contrast (PC) microscopy is non-invasive and creates contrast in optically transparent cells, but PC images are subject to intrinsic artefacts, namely the “halo effect” – bright regions around object edges. This means thresholding-based segmentation methods alone are insufficient to identify cells. We propose a method for localising cells in PC images of epithelial monolayers at a range of densities to generate growth curves non-invasively.

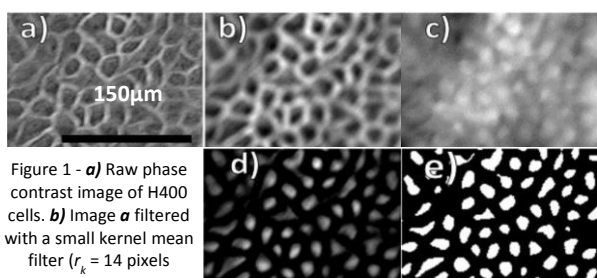


Figure 1 - **a)** Raw phase contrast image of H400 cells. **b)** Image **a** filtered with a small kernel mean filter ($r_k = 14$ pixels = $5\mu\text{m}$) retaining bright intercellular spaces with dark centres. **c)** Original image **a** filtered with a large kernel mean filter ($r_k = 80$ pixels = $31\mu\text{m}$). Cell containing regions are brighter than the surrounding regions. **d)** Image **b** subtracted from image **c**. Cell containing regions now appear brightest and Otsu's thresholding is applied to obtain image **e**. The contrast has been enhanced in all images for improved reproduction.

Firstly, two mean filters with circular kernels of different radii, r_k , are applied to the PC image. When r_k is smaller than that of a cell, cells retain bright edges and a relatively dark centre (fig.1b). Conversely, when r_k is larger than the average cell, cell centres become brighter than the margins (fig. 1c). Imposing a minimum pixel greyscale value of 0 and subtracting the small r_k image from the large r_k image results in an image where cell containing regions are brightest (fig. 1d), and therefore cells may be located and counted by applying a global threshold method such as Otsu's (fig. 1e) [1].

A second step verifies that each binary object corresponds with a cell, since incorrectly identified regions will bias cell counts. To this end, 32 features describing the morphology of the binary segmented regions and their greyscale properties in the corresponding regions of the original image are calculated and reduced to 4 features using Principal Component Analysis. Segmented regions are then classified as "true" (real cell) or "false" cells (incorrect segmentation) by applying k-means clustering (with $k = 2$). Classification success was evaluated by comparison with a set of 10 images of cultures at a range of densities in which segmentations had been manually classified. We used the F-score as a combined measure of classification precision and recall, which ranges between 0 and 1 (best value). This approach generated an F-score > 0.9 for all images analysed.

Our method was validated by culturing H400 keratinocytes [2] in media containing increasing concentrations of foetal calf serum (FCS), a supplement required for cell proliferation. The average number of cells in 20 images acquired at random locations in the culture dish was determined using the approach described here and repeated at six time-points between 48-120 hours post-seeding to generate growth curves. Data supported the validity of the image analysis approach as H400 cell proliferation rates were dose dependently associated with FCS concentration.

References

- [1] Otsu, N. 1975. A threshold selection method from gray-level histograms. *IEEE Trans. Sys., Man., Cyber.*, **9**, 146-165
- [2] SS Prime *et al.* 1990. The behaviour of human oral squamous cell carcinoma in cell culture. *J. Pathol.*, **160**, 259-269

Simulation of Light Field Imaging for Optimal Design

C J Meah¹, R J Marshall¹ and I B Styles¹

¹School of Computer Science, University of Birmingham, UK.

c.j.meah@pgr.bham.ac.uk

A conventional camera uses a lens to focus rays of light onto sensor pixels. The pixels record the intensity of the ray's incident upon them, but any directional information is lost. Furthermore, a single plane of the scene is captured in focus, with objects away from this plane blurred in the image.

A light field camera introduces a microlens array between the main lens and sensor of a conventional camera [1]. Rays that would have met on a sensor pixel in a conventional system are now split by a microlens into directional bins. This means that both the directional information and intensity of a ray are now recorded. Although this extra information is captured at the expense of spatial resolution, it allows to change the focus, aperture, and viewpoint of an image in post-processing. This ability to capture the 3-D information of a scene in a single acquisition makes light field imaging a powerful technique for many application domains.

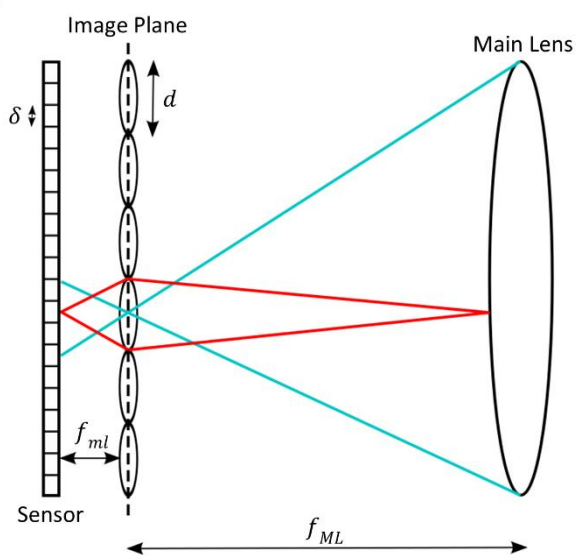


Figure 8- Schematic representation of a light field camera

Although commercial cameras exist [2], for optimal performance in specific applications a custom camera is usually required. However a light field camera is often difficult to build and to optimise. A simulation tool has been created utilising ray tracing techniques which allows for the digital exploration and optimisation of light field camera design, aiding the exploration of applications.

Alongside this simulation software, a rendering toolbox has been created which can render images from a light field image (from original or focused light field cameras). This rendering toolbox contains custom-made reconstruction methods for depth-mapping, and light field limited-angle tomography.

Since light field data processing is computationally intensive, the MATLAB Parallel Computing Toolbox (MATLAB, **MathWorks, Cambridge, UK**) has been utilised to improved speed of computation. Finally, the combining the simulation and rendering toolboxes has led to simulation informed tomography, which has implemented alongside existing methods for comparison.

References

[1] Ng, Ren, et al. "Light field photography with a hand-held plenoptic camera." *Computer Science Technical Report CSTR 2.11* (2005).

[2] <http://www.raytrix.de/>

Investigating the potential for plenoptic imaging of the retina

Richard Marshall¹, Chris Meah¹ and Iain Styles¹

¹PSIBS Doctoral Training Centre, School of Chemistry, University of Birmingham, UK.

r.j.marshall@pgr.bham.ac.uk

Plenoptic imaging is a relatively new imaging modality, in which both the angular and positional information of the incident light rays are recorded by a single image. This is achieved by placing a microlens array between the objective lens and the sensor inside the imaging system (Figure 1). Rays of light that would be incident on a single point are then split by the microlenses, interacting with different pixels on the sensor depending on their angle of incidence. The aim of this investigation is to examine how plenoptic imaging can improve fundus photography.

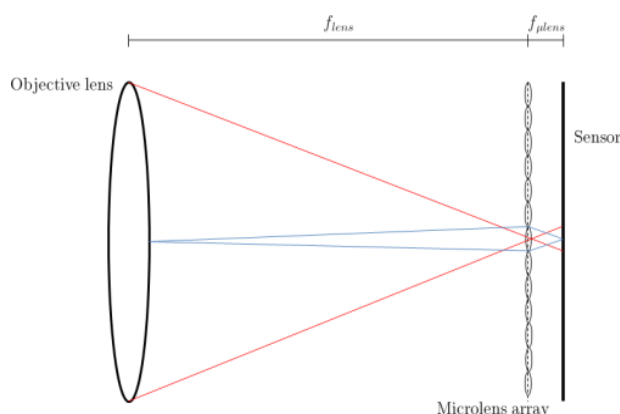


Figure 1: A schematic diagram of a plenoptic camera in the traditional configuration

The aim of the investigation was to look at the scattering of light between the retinal surface and the retinal pigment epithelium (RPE). Monte Carlo simulations were performed using MCML [1], a multi-layered Monte Carlo modelling software package. The first experiment targeted only ballistic photons being transmitted to the RPE. As plenoptic imaging can only determine the depth from the point of last scatter, if no or only a very small proportion of the light rays travel unscattered to the RPE, then a quantitative depth will not be able to be

determined. This is significant in retinal imaging, as diseases such as diabetic macular edema (DME) causes thickening of the retinal tissue. If a quantitative retinal thickness could be determined, this would significantly aid in the early detection of DME. The second experiment examined the angular reflectance of the light at the surface of the retina. By then repeating the experiment but by changing the retinal thickness, if the angular distribution is a function of the retinal thickness then this could be used as a method to diagnose DME.

The results of the first experiment showed conclusively that a quantitative depth could not be achieved by using ballistic photons, as no more than 0.35% of photons were ballistic. The second experiment showed no significant difference in the angular distribution when the retinal thickness was varied. This indicates that retinal thickness is not a function of reflected angular distribution of the light. However, this indicates that a good surface image of the retina could be achieved, independent of retinal thickness. This would be useful for diagnosing diseases such as glaucoma, in which the cup-to-disc ratio is used for diagnosis.

References

[1] L. Wang, S. L. Jacques, and L. Zheng. 1995. MCML - Monte Carlo modeling of light transport in multi-layered tissues. *Computer methods and programs in biomedicine* **47.2**, 131-146.

SuSi : A Monte Carlo model of a novel proton CT Scanner using Geant4

Tony Price^a, Jon Taylor^b, Michela Esposito^c, Gavin Poludniowski^d,
Jeyasugiththan Jeyasingam^e

^a School of Physics and Astronomy, University of Birmingham, B15 2TT, UK

^b Department of Physics, University of Liverpool, Oxford Street, L69 7ZE, UK

^c Laboratory of Vision Engineering, School of Computer Science, University of Lincoln, LN6 7TS

^d Centre for Vision, Speech and Signal Processing, University of Surrey, GU2 7XH, UK

^e Department of Physics, University of Cape Town, 7701, South Africa

Abstract

Proton radiotherapy uses beams of high energy protons to treat cancer. It is specifically used for cancers in children and near delicate structures due to the ability of delivering a highly focused dose to the cancer volume. The PRaVDA consortium are building an imaging device to image the patients with protons and form a proton Computed Tomography (pCT) image which will reduce the uncertainties on the treatment and further enhance patient care. Here we present the results of a Monte Carlo simulation of a novel proton Computerized Tomography instrument. We will give a brief overview of our pCT system whilst primarily focusing on our Monte Carlo modelling efforts using Geant4 to develop a full scale detector model to replicate our final design, the PRaVDASuperSimulation (SuSi). We will outline the results from modelling the sensors' response and present a reconstructed proton CT image. We will also stress the importance of having a cluster such as BlueBEAR to perform these studies by illustrating the real time benefits of running the simulation compared to a single core machine.

Introduction

Proton radiotherapy, first proposed by Robert Wilson in 1946 (1), uses external beams of high energy protons to treat cancer. Whilst the first patients were treated at Berkeley Radiation Laboratory (California, US) in 1954 (2), it was not until 1989 at the Clatterbridge Centre for Oncology (Wirral, UK) when patients were treated in a hospital environment (3). Following the initial slow uptake, the number of proton therapy centres has increased rapidly over recent years (4) with many more sites currently in the planning stages, including two centres in the UK.

The energy deposition profile of a high energy proton has a characteristic shape known as the Bragg Peak. Initially, the proton will deposit just a small fraction of its energy per unit length, known as the proton stopping power in units of MeV/cm. As the proton loses energy, the amount of energy it deposits per unit length increases. This increase is slow at first but becomes much more rapid just before the proton loses all of its energy. This leads to a large proportion of the protons energy being deposited in a very small region at a particular depth in a material. The range a proton travels in a material is dependent on two things, the initial energy of the proton and the material it is travelling through. If we know the location of a tumour within a patient and the body tissues the protons need to travel through before the tumour, it is possible to deposit a huge amount of energy in a tumour whilst sparing healthy tissues surrounding it.

To ensure that the proton stops in the tumour and not healthy tissue a patient is imaged to determine the compositions and locations of the surrounding body tissues. Conventionally, this is achieved using Computerized Tomography (CT) which uses beams of x-rays to measure the electron density of the body tissues. The underlying physical processes which govern the interactions of x-

rays and protons are very different and the conversions from electron density to proton stopping powers are non-trivial. The generally accepted uncertainty on the range of the protons is 3.5 % (5) with up to 2 % arising from the conversion alone (6). If a patient could be imaged directly using protons we would be able to measure the proton stopping powers of all the body tissues directly and reduce this uncertainty dramatically. The Proton Radiotherapy Verification and Dosimetry Applications (PRaVDA) consortium are designing, building, and testing the world's first all solid state proton CT (pCT) device. Here we present the Monte Carlo model that has been developed to assist in the design of the device and predict the quality of the final images.

The PRaVDA Device

During a pCT, the position, direction and energy of every single proton must be measured before and after the patient to maximise the resolution of the final image. This will be achieved by pairing technologies developed at the Large Hadron Collider with large CMOS sensors. An illustration of the PRaVDA device, showing the strip trackers and CMOS sensors is given in Figure 9.

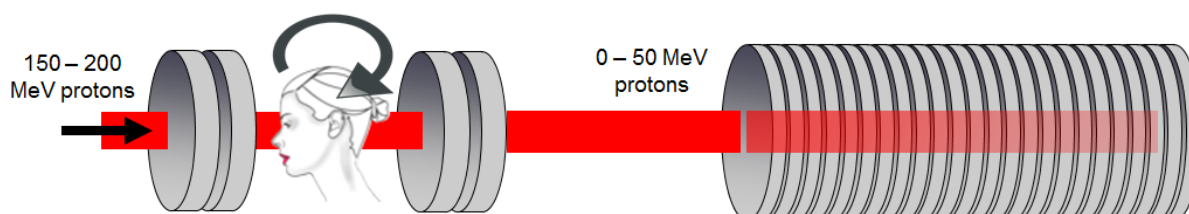


Figure 9 - Illustration of the PRaVDA device showing the strip tracking sensors around the patient (left) and the CMOS range telescope (right). The red line represents a beam of protons.

Silicon Tracking Sensors

The positions of the protons are tracked into the patient with two banks of strips sensors. Each bank of sensors contains three strip sensors orientated at 60 degrees to each other. A strip will fire in each sensor and the location where the three strips overlap provides a hit position of the proton. The hit positions in the sensors are projected onto the patient surface to provide an input position. There are two identical banks of sensors downstream of the patient which will allow the exit location of the proton from the patient to be reconstructed using the same methodology. The incident and exit positions are used to estimate the path of the proton through the patient.

CMOS Range Telescope

The CMOS Range Telescope is constructed of 24 layers of CMOS sensors interlaced with 1 mm of Perspex. The CMOS has a pixel pitch of 200 microns and each layer has an area of 14x10 cm². The proton track from the tracking sensors will project onto the front face of the Range Telescope and hits within the first layer will be paired up with each track. A dedicated tracking algorithm will then use the position and signal size measurements obtained from the CMOS to track each proton until it comes to a stop. The range of the proton within the Range Telescope will be converted into a water equivalent path length and the energy lost by the proton through the patient can be calculated.

Phantom Design

Until this point, the object being imaged has been referred to as the patient. Whilst this will be the case in a final pCT, during the initial proof of principle stage the patient will be a Perspex phantom. The Perspex phantom will be a spherical object which will have inserts of materials with the same compositions as human tissue to allow the performance of the device to be quantified.

Novel Reconstruction Algorithm

In conventional CT reconstruction the image is reconstructed using a filtered back projection algorithm. This involves taking an image of the patient at multiple angles, transforming the image into fourier space, filtering out certain spatial frequencies and then projecting the resulting image back along the path the x-rays took through the patient. This is then repeated at multiple angles and an image is formed. Filtered back projection is not suited for pCT as protons do not travel in straight lines through the patient like x-rays would and this reduces the image resolution. The PRaVDA consortium have written a new algorithm, better suited for pCT known as backprojection-then-filtering as outlined here (7). SuSi allows the performance of this new algorithm to be tested.

SuSi: An Overview

Marrying together different detector types, tracking high energy protons through 36 layers of sensors and a patient, and reconstructing an image using a novel reconstruction algorithm requires the optimisation of a huge number of properties. These include but are not limited to; the spacing between each tracking module; the size of the patient region; thresholds in the sensors; phantom design; detector sizes; readout rate required to track individual protons; the location of sensitive electronics and shielding to prevent radiation damage, and the amount of Perspex in the Range Telescope to contain the protons but not affect the image quality.

A detailed Monte Carlo simulation, namely the PRaVDASuperSimulation or SuSi for short, has been developed to fully optimise the PRaVDA device due to its immense complexity. This uses the Geometry and Tracking (Geant4) (8) software package developed, tested and validated for use in High Energy Physics. The simulation currently has 46 classes written in C++ to allow each component of the PRaVDA device to be modelled, parameters changed and optimised, and the interplay between changing different parts of the system on other aspects to be investigated.

Initial tests of the final device will be conducted using the University of Birmingham Cyclotron. This cyclotron has a maximum energy of 40 MeV and beam size of 5 cm. The final tests will be conducted at the iThemba LABS, a medical facility in SA which has a beam energy of 191 MeV used to treat patients. The infrastructure at these two facilities are very different and the protons which interact with the device have different energies, beam divergences and associated secondary particles. SuSi allows the PRaVDA device to be simulated at both of these locations, ensuring that the correct incident particle profiles are modelled.

When a particle interacts with the silicon, it will deposit some energy via ionisation. This liberates electrons from the silicon which diffuses through the sensors and is collected by the readout electronics. SuSi takes into account the differences in the charge spreading in the tracking sensors and the CMOS sensors and contains algorithms for realistic charge spreading which yields correct signal sizes and cluster sizes as collected with test sensors. The output from the simulations has been used to develop the tracking code for both the strip trackers and the range telescope and the impact on track resolution has been studied for various sensor positions.

The resulting data from the simulation allows the testing and tuning of the reconstruction algorithm. SuSi has the potential investigate the main factors which affect the reconstructed image quality by turning on and off properties such as multiple scattering, beam energy spreads, the effect of non-perfect detectors, noise in the detectors and uncertainties in the construction of the body tissues.

Results

Beam Line Models

The profiles of the protons have been extensively tested at both the Birmingham and iThemba locations and the simulations tuned to match the data with excellent precision. At iThemba, the range of the protons can be degraded by reducing the energy of the incident protons. This is achieved by inserting graphite wedges upstream of the final treatment nozzle. Figure 10 illustrates the excellent agreement between data and SuSi output for four proton beams where the energy has been degraded by differing amounts. Similar plots have been observed for the model describing the Birmingham cyclotron alongside excellent agreements in lateral beam profiles at both locations.

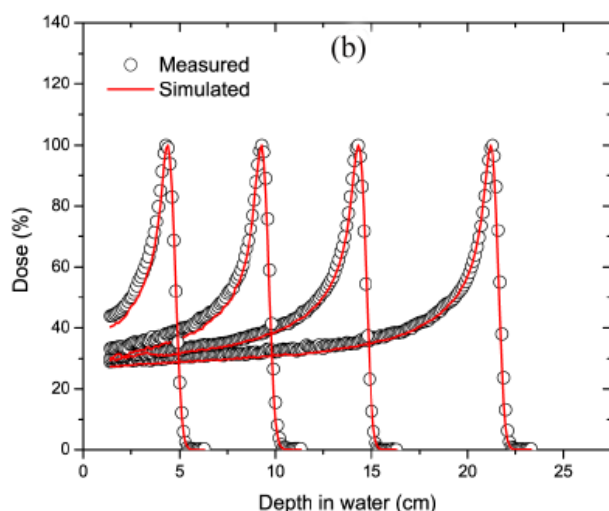


Figure 10 - Reconstructed Bragg peaks for various beam energies at iThemba showing the comparison between data and simulation.

improved agreement at 191 MeV.

CMOS Range Telescope

Data taken with a 36 MeV proton beam at the University of Birmingham incident upon a single CMOS sensor close in design to the final PRAVDA CMOS sensor is compared against the output from SuSi in Figure 12. A very low current of protons were incident upon the sensor, enabling the measurement of the energy deposited by individual protons with high precision. Using realistic charge spreading algorithms, threshold functions, gain and noise parameters the output from SuSi is in excellent agreement with the data. This demonstrates the ability of SuSi to predict the behaviour of both the proton and the sensor response to the proton. This allows for a model of the full CMOS Range Telescope to be developed and optimised with high certainty and belief in the results.

Strip Trackers

The signal size in the strip trackers using the full energy, 191 MeV iThemba proton beam can be seen in **Error! Reference source not found.**. The signal size is the sum of the charge collected across neighbouring strips. Also shown in **Error! Reference source not found.** is the resulting signal size obtained from SuSi using the full energy iThemba model. The difference between data and simulation is less than 10%. The 191 MeV beam will deposit the smallest signal in any of our sensors and the lower energy protons demonstrate an improved agreement. The charge spread algorithm is being refined and preliminary results yield a further

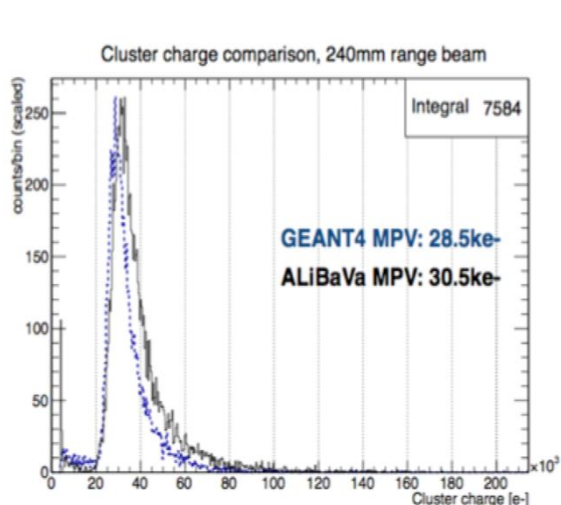


Figure 12 - Signal size in the strip tracking sensor compared to SuSi output for the 191 MeV iThemba proton beam

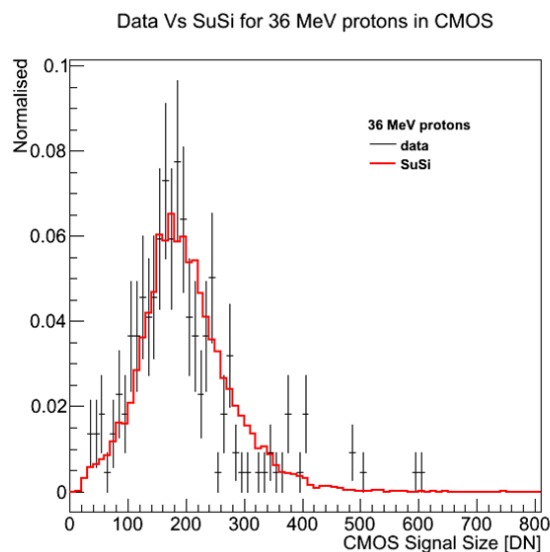


Figure 12 - Signal size in one CMOS range telescope sensor for 36 MeV protons from the University of Birmingham compared with simulation

Reconstruction

The slice of a fully reconstructed pCT slice of our phantom using data from SuSi is presented in Figure 13. Whilst SuSi has presented the ability to accurately model the sensor responses the reconstruction uses perfect truth information with no resolution or inaccuracies on the proton positions. This was done to present an initial verification of the reconstruction algorithm and allows the effect of the introduction of the sensors onto the image resolution to be isolated and evaluated. Both SuSi and the reconstruction algorithm are still being developed this will be assessed in future work.

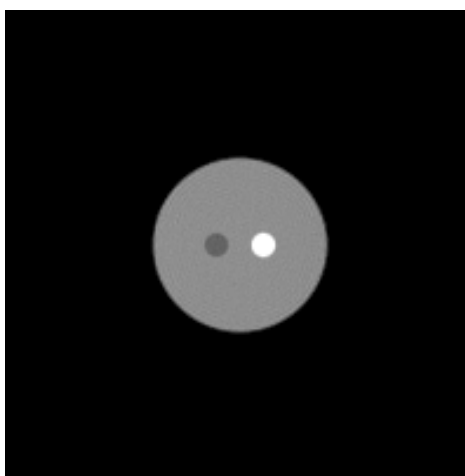


Figure 13 - Reconstructed slice of phantom using back projection filtering showing two inserts using perfect detector information from SuSi

Run Time Statistics

It is believed that a full pCT image will require 3×10^8 fully reconstructed protons. Here we present the run time statistics of a pCT simulation from SuSi which yielded 10% of the required reconstructed protons.

A pCT image will require data to be taken with the patient rotated through 180 degrees in steps of 1 degree. At each of these angles 2×10^6 protons were generated and fully reconstructed using on average 11h34m CPU time and producing 5GB of data each. For this dataset, each angle of the simulation used a single node yielding a total of 2100 CPU hours and 900 GB of data. Using BlueBEAR these simulations were completed in just 3 days, a decrease in real time on a single CPU of 3000%.

Discussion and Future Plans

We have presented here a fully functioning model of the PRaVDA pCT instrument and the ability to test it using two realistic sources of radiation including all secondary particles and validated initial conditions. The simulation contains realistic sensor characteristics which yield an output in excellent agreement with measured signals. This information has been used to optimise the device and test a novel reconstruction algorithm.

Whilst SuSi has demonstrated excellent results thus far it is still under development. Improvements to the charge sharing algorithms, additional components, and enhanced noise behaviour in the sensors are all planned. Alongside these changes the algorithms will be optimised for speed and the output data filtered to reduce CPU time and storage space in preparation of a full simulated dataset.

References

1. *Radiological Use of Fast Proton*. **Wilson, Robert R.** 1946, Radiology, pp. 487-491.
2. *Pituitary Irradiation with High-Energy Proton Beams A Preliminary Report*. **Tobias, C. A.** 1958, Cancer Research, pp. 121-134.
3. *The Clatterbridge Proton Therapy Facility*. **Bonnett, D E and Kacperek, A and Sheen, M.** 1990, Paul Scherrer Institute, p. 143.
4. **Goethals, P E and Zimmermann, R.** *Proton Therapy World Market Report Edition 2013*. 2013.
5. *Comprehensive analysis of proton range uncertainties related to patient stopping-power-ratio estimation using the stoichiometric calibration*. **Dong, Ming Yang and X Ronald Zhu and Peter C Park and Uwe Titt and Radhe Mohan and Gary Virshup and James E Clayton and Lei.** 2012, Physics in Medicine and Biology, p. 4095.
6. *Range uncertainties in proton therapy and the role of Monte Carlo simulations*. **Paganetti, H.** 2012, Physics in Medicine and Biology, p. R99.
7. **Poludniowski, G.** The Lincoln Repository. [Online] <http://eprints.lincoln.ac.uk/14745/>.
8. *Geant4 : a simulation toolkit*. **Agostinelli, S and Allison, J and Amako, K.** 2003, Nuclear Instruments and Methods in Physics Research Section A: Accelerators, Spectrometers, Detectors and Associated Equipment, pp. 250-303

Characterisation of Chemical Ordering in Palladium-Iridium Nanoalloys

Jack Davis¹, Leonid Rubinovich², Micha Polak² and Roy Johnston¹

¹School of Chemistry, University of Birmingham, UK.

²Department of Chemistry, Ben-Gurion University of the Negev, Beer Sheva, Israel.

jxd231@bham.ac.uk

Nanoalloys (NAs) are nanoparticles composed of two or more metallic elements. The combination of metals can produce materials with well defined, controllable properties, as NA properties depend not only on size and shape but also on the composition and ordering of elements. Palladium-Iridium NAs have been investigated for use in several catalytic systems, including tetralin hydroconversion[1].

In order to rationalise these nanoalloying effects their structural characterisation is essential. Global optimisation on small Pd-Ir nanoalloys has been previously conducted[2], this is, however, infeasible for structure larger than 20 atoms. For larger NAs it can be assumed that structures will be similar to that of the bulk alloy. It is, therefore, only important to find the correct chemical ordering for a particular size nanoalloy structure.

The Free-Energy Concentration Method (FCEM), using Coordination-Dependent Bond Energy Variations (CBEV), is a statistical mechanical method for prediction of chemical ordering in NAs of up to 1000 atoms[3]. Using newly computed energetics, CBEV/FCEM has been applied to study of compositional ordering in Pd-Ir truncated octahedra.

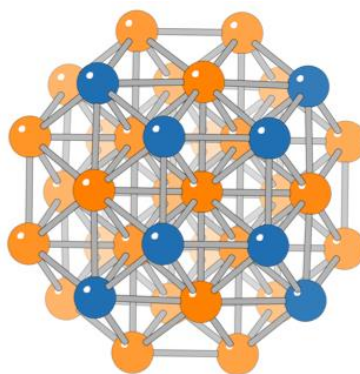


Figure 1: Lowest energy predicted ordering for Pd₈Ir₃₀

References

- [1] L. Piccolo, S. Nassreddine, M. Aouine, C. Ulhaq and C. Geantet, *J. Catalysis*, 292, **173**, (2012).
- [2] J. B. A. Davis, S. L. Horswell and R. L. Johnston, *J. Phys. Chem. A*, **118**, 208-214, (2014).
- [3] M. Polak and L. Rubinovich, *Surface science*, 584, 41, (2005).

Global Optimisation of Hydrated Sulfate Clusters

Lewis C. Smeeton¹, Mark T. Oakley¹, Sven Heiles², Evan Williams² and Roy L. Johnston¹

¹School of Chemistry, University of Birmingham, UK.

²Department of Chemistry, University of California, Berkeley, UK.

lcs137@bham.ac.uk

The Hofmeister series ranks the ability of ions to affect a number of phenomena in physical chemistry[1], including surface tension, protein solubility and stability and bubble formation to name a few. SO₄²⁻ is a Hofmeister ion which sits at the far “kosmotropic” end of the series, meaning that it increases surface tension and decreases protein solubility. Despite the relative importance of the series, its exact chemical origin remains unclear, with evidence supporting both direct ion interaction and long range effects of the ion on solvent structure. Infrared photodissociation (IRPD) spectroscopy of gas phase hydrated sulfate ions provide information as to the hydrogen bonding of waters at the surface and interior of the cluster[2]. IRPD spectra of size selected SO₄²⁻-(H₂O)_n suggest that for $n \leq 43$, all the waters in the cluster are hydrogen bonded to either the sulfate or another water. This contrasts with both water clusters of comparable size and at the surface of the bulk, where a number of waters exhibit “free”, non-bonded OH-groups.

The aim of our study: Can simulation detect the size-dependent appearance of free OH-groups in hydrated sulfate clusters by searching the potential energy surface?

In order to model the potentially large system sizes, the sulfate ion and waters were initially modelled as rigid-bodies interacting through pairwise potentials. A Basin-hopping monte-carlo algorithm[3] with rigid-body translational and rotational moves, and a novel hydrogen-bond cage optimisation move set was used to search for low-lying energy minima. The lowest energy minima were then re-optimised at the density functional theory level, and their vibrational normal modes were computed. We demonstrate that even at the rigid-body potential level, we are able to replicate some of the behaviour of the hydrated sulfate cluster, with simulation predicting that free OH-groups appear around $n = 33$ waters.

References

- [1] W. Kunz, P. Lo Nostro, and B. W. Ninham, *Curr. Opin. Colloid. In*, 2004, **9**, 1-18
- [2] J. T. O’Brien, J. S. Prell, M. F. Bush and E. R. Williams, *JACS*, 2010, **132**, 7811-7819
- [3] D. J. Wales and J. P. K. Doye, *J. Phys. Chem. A*, 1997, **101**, 5111-5116

Ordinal Regression Based on Learning Vector Quantization

Fengzhen Tang and Peter Tino

School of Computer Science, University of Birmingham, UK.

fxt126@cs.ham.ac.uk

Ordinal regression problems are multi-class classification problems where a natural order among categories can be observed [1] and they are recently receiving considerable attention [2,3]. In this abstract, we propose a new ordinal regression algorithm based on Learning Vector Quantization, which is a prototype-based classification algorithm using prototypical examples to represent classes. In the proposed algorithm, the ordinal information in the class label is utilized in the selection of the prototypes to be adapted, as well as in the determination of how to update the selected prototypes. The proposed algorithm guarantees that the prototypes are organized in order.

The proposed ordinal regression algorithm is developed based on Generalized Matrix Learning Vector Quantization, extending the work in [2]. The algorithm updates prototypes in pairs by attracting the closest correct one while repulsing the closest incorrect one. Moreover, the full adaptive metric in the distance measure allows the correlations between different features and their importance for the classification scheme to be taken into account. An advantage of this algorithm is that it applies the generalized learning rules, which is derived from an explicit cost function. This algorithm has been extended for ordinal regression [2] by updating several pairs of prototypes each time in a weighted scheme. However, the updating of the prototypes to ensure the ordering are sensitive to the width parameters of the Gaussian weighing functions. We propose to update all the identified correct and incorrect prototypes cumulatively, in which the ordering of the prototypes can be explicitly expressed in the updating rule derived from the proposed cost function. Moreover, we propose to learn the width parameters automatically during training. Experimental results show that our ordinal regression algorithm are competitive to the ordinal regression algorithm presented in [2] and much better than the original GMLVQ, which ignores the ordering information in the class labels.

References

- [1] Jaime S. Cardoso and Joaquim F. Pinto da Costa. Learning to classify ordinal data: The data replication method. *Journal of Machine Learning Research*, 8:1393–1429, 2007.
- [2] Shereen Fouad and Peter Tino. Adaptive metric learning vector quantization for ordinal classification. *Neural Computation*, 24(11):2825–2851, 2012.
- [3] Chun-Wei Seah, Ivor W. Tsang, and Yew-Soon Ong. Transductive ordinal regression. *IEEE Transactions on Neural Networks and Learning Systems*, 23(7):1074–1086, 2012.

Extrusion of a Vortex Lattice

Jonathan S. Watkins,¹ and Nicola K. Wilkin²

¹School of Physics and Astronomy, University of Birmingham, UK.

jwatkins@theory.bham.ac.uk

²School of Physics and Astronomy, University of Birmingham, UK.

n.k.wilkin@bham.ac.uk

Solid vortex matter presents a “solid” whose density can be varied by up to an order of magnitude while the crystal symmetry is unchanged. The consequent unconventional metallurgy of the vortex lattice has been largely unexplored. In this Letter, we show there is a dramatically different regime of plastic deformation compared to ordinary solids. When the plastic deformation occurs with a significant change in *density*, as well as relaxation in shear stresses, we show there is a novel steady state regime of this driven nonequilibrium system. This flow utilises two distinct populations of mobile dislocations. One population facilitates the relaxation of density; a second, more conventionally, aids the relaxation of shear stresses which are concentrated at the boundaries.

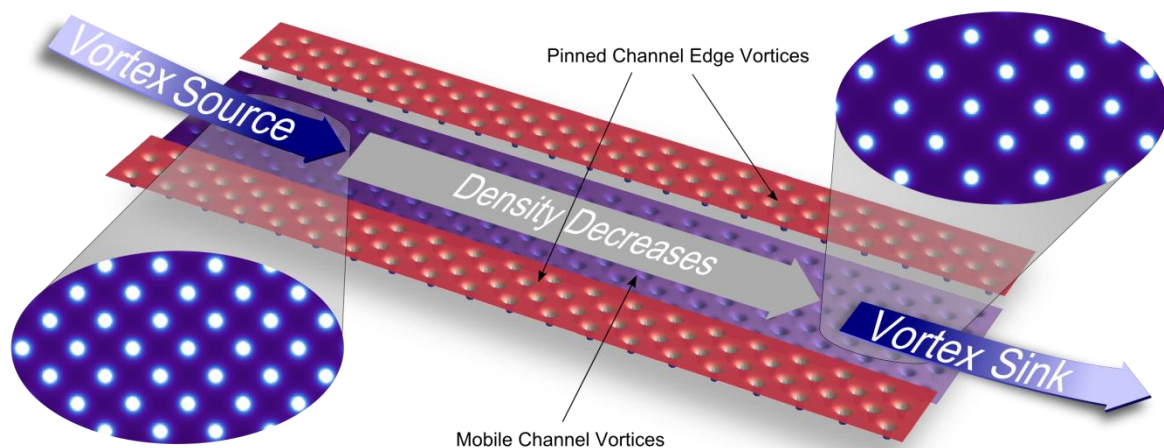


Figure 1: Model of a thin channel superconductor with an imposed magnetic field gradient $B(x)\hat{z}$. Mobile vortices from a high density source are free to move along the channel under the action of a vortex magnetic pressure gradient. The channel edges are defined by pinned vortices.

References

- [1] A. Pruyboom, P. H. Kes, E. van der Drift, and S. Radelaar. Phys. Rev. Lett., 60:1430–1433, Apr 1988.
- [2] P. H. Kes, N. Kokubo, and R. Besseling. Physica C: Superconductivity, 408(0):478–481, 2004.
- [3] R. Besseling, P. H. Kes, T. Dröse, and V. M. Vinokur. New Journal of Physics, 7(1):71, 2005.
- [4] H. J. Jensen. In Phase Transitions and Relaxation in Systems with Competing Energy Scales, volume 415, pages 129–185, Netherlands, 1993. NATO, Kluwer Academic Publ.
- [5] C. Reichhardt, C. J. Olson, R. T. Scalettar, and G. T. Zimányi. Phys. Rev. B, 64:144509, Sep 2001.
- [6] A. Amir and D. R. Nelson. Proc. Natl. Acad. Sci. USA, 109(25):9833–9838, JUN 19 2012.

Numerical study of the structural response of S460 & S690 Beams

Gkantou, M.¹, Baniotopoulos, C.¹, Theofanous M.¹, Hemida H.¹

¹School of Civil Engineering, University of Birmingham, UK.

m.gkantou@bham.ac.uk

Increasing demands for light and sustainable structures together with the technological advances in material science brought high strength steel (HSS) into the construction market over the last decades. HSS's principal benefit is the weight reduction which is achieved thanks to its high yield capacity. A lighter structure, apart from implying aesthetically more elegant and iconic solutions, implies smaller member sizes and foundations which in turn lead -both directly in less material used and indirectly in lower transportation workloads - to lower CO2 emissions and energy use.

Even though HSS has been widely applied in automobile, crane and offshore engineering [1] [2] [3], restricted market availability and structural behaviour considerations have limited its use in structural engineering. The main aim of the current study is to contribute to the research on the cross-sectional response of high strength steel beams which is inadequately covered in codes around the world. The objectives include the development of non-linear numerical models for the verification of experimental results of HILONG project and the subsequent execution of parametric studies. More particularly, 3pt (point) and 4pt bending laboratory tests were replicated by nonlinear finite element models which managed to accurately verify the ultimate load capacity and post-ultimate response. All modelled components employed square (SHS) and rectangular (RHS) hollow sections in grades S460 and S690. After the validation of the models, parametric studies were conducted to determine the structural response of beams with various cross-section slenderness and aspect ratios and subsequently assess the suitability of current Eurocode classification limits.

The current study utilized the general purpose finite element package ABAQUS. Both linear (Eigenbuckling) and non-linear (Riks) analysis [4] were performed during the research, whilst the adopted material properties were derived from coupon tests data conducted within HILONG project

References

- [1] Willms, R. (2009) High strength steel for steel constructions. Nordic Steel Construction Conference, Malmo, Sweden, pp. 597–604
- [2] J. Billingham, J.V. Sharp, J. Spurrier, P.J.K. (2003) Review of the performance of high strength steels used offshore
- [3] Tanabe H, Miyasaka A, Yamazaki K, Iwasaki T, Akada H. High strength steel tubes for automobile door impact beams. In: Nippon Steel Technical Report No. 64, 1995
- [4] Hibbitt, Karlsson, Sorensen Inc. ABAQUS, (2010) ABAQUS/Standard user's manual volumes I–III and ABAQUS CAE manual. Version 6.10. USA: Pawtucket

Effect of floodplain on the flow in asymmetric compound open channels

Marjan Molaie¹, Hassan Hemida, Xanon Tang

¹School of Civil Engineering, University of Birmingham, UK

1Mxm381@bham.ac.uk

Vegetation generally appears at the edge of the floodplain and main river channel, both habitually and by design to prohibit deterioration. There is little known about the effect of such vegetation along floodplains on flow structures and flow resistances. Also the interaction between a river channel and its floodplain flows is complex, generating various type of secondary flow and eddies. The effect of these secondary flows on the water discharge and shear stress is also unrevealed. This research, therefore, is to investigate the effect of both emergent and submerge vegetated floodplain on the flow characteristics by employing computational fluid dynamics (CFD). To achieve this aim, the first step will be to develop a 3D numerical model to understand the behaviour and effect of both the emerged and submerged vegetation on the flow characteristics. Part of this is to investigate the effect of cross section on the mean flow velocity, the depth average velocity, boundary shear stress and turbulence characteristics of the flow in smooth and rough compound channels.

In this work unsteady Reynolds Averaged Navier–Stokes equation (RANS) and Large Eddy Simulation (LES) will be implemented to investigate the flow phenomena in symmetric and asymmetric open compound channel with and without vegetation. The model will first be validated in two cases: flow in a symmetric compound open channel with varying width ratio and without vegetation with two different configurations of channels, and flow in an ‘asymmetric’ compound open channel without vegetation. The experimental set of data taken from Knight and Demetriou (1983), the Flood Channel Facility (FCF) by Knight (1992) and Atabay (2001) will be used to examine the novel boundary condition for the model [1].

In the next step the developed model will be applied to a symmetric compound open channel with different vegetation density in which LES will be done for an open channel flow through submerged vegetation with a different height ratio (water depth to plant or vegetation height). In my presentation I will show the comparison with the experimental work and the initial results of the LES simulations.

References

[1] Tang.X, Knight.Donald W,Lateral Depth-average Velocity Distributions and Bed Shear Stress in Rectangular Compound Channels, Journal of Hydraulic Engineering, 1337-1342, (2008).

Effect of Ballast Shoulder Height on a passenger Trains Slipstreams and Wake, A Computational Fluid Dynamics study

First J. Morden, Second H. Hemida and Third C. Baker
School of Civil Engineering, University of Birmingham, UK.

jam239@bham.ac.uk

Abstract

This paper presents a Computational Fluid Dynamics (CFD) study on the effect ballast shoulder height has on the slipstream pressures and velocities produced by a passenger train. Results for three single sided ballast shoulder heights are presented with data from CFD and model scale experiments. The train being investigated is a 1/25th scale class 43 High Speed Train (HST). The train comprises of four cars, a power car, two passenger cars and a towed power car as the tail. The CFD investigation uses the Delayed Detached Eddy Simulation (DDES) approach. The DDES approach uses the Spalart-Allmaras turbulence model. Results showed that the DDES approach produced good correlation with the experimental results for the slipstream pressure profiles at all measurement locations. Slipstream velocity profile predictions did not show the same level of correlation at all measurement locations. As ballast shoulder height was increased, pressures and velocities within the slipstream reduced, this matched with experimental data collected. Visualisation of the flow showed this reduction in pressure and velocity occurs due to an increase in area for the vortices to move about and dissipate within. As ballast shoulder height is increased vortices released from the trains under-body roll down the ballast shoulder side. The shedding of vortices is found to be caused by an oscillation of the flow within the trains under-body, this oscillation becomes skewed with the increase in ballast shoulder height leading to an increase in the number of vortices shed. The wake of the train is also affected by the ballast shoulder by being drawn towards the shoulder side.

Introduction

The velocities and pressures within a trains slipstream are important flow characteristics that have an effect on the safety of both passengers and nearby personal such as railway workers. Within the Technical Specifications for Interoperability (TSI) [1] requirements are specified for the maximum train slipstream velocities. This range of ballast shoulder heights may lead to variations in both the measured pressures and velocities, providing an opportunity for a train manufacturer to achieve a pass on their train by the correct choice of testing location. Research presented within this paper forms part of “The measurement of train aerodynamic phenomena in operational conditions” research project being conducted within the University of Birmingham and funded by the UK Engineering and Physical Sciences Research Council, EPSRC. This paper reports on the effect ballast shoulder height has on velocities and pressures within the slipstream of a passenger train.

The train used within this research is a class 43 high speed train (HST), this train was chosen due to the active use by network rail of a specially adapted HST with sensors to measure aerodynamic pressures over its surface that will provide data towards the overall research project. The HST within this research was 1/25th scale and comprised of four cars, a power car, two passenger cars and a towed power car (tail). This model matches a scale model used at the universities moving model rig

(MMR), data collected at this rig is compared to CFD results. The CFD approach chosen for this investigation is DDES [2]. The DDES approach relies upon the Spalart-Allmaras turbulence model [3] within the RANS based regions.

Results are compared between the experimental and the CFD results at two measurement locations, location A which is situated at 3m from the centre of the rail (COR) and 0.2m above the top of the rail (TOR) and location B situated at 2.37m and 2.25m from COR and TOR respectively. Research conducted by Hemida and Baker [4] Found that the slipstream of a train varies greatly in its strength depending on its height above TOR, their results show that an increase from 0.2m to 1.5m results in a 50% drop in slipstream velocity.

Moving Model Rig Experiment

The moving model rig is a facility owned by the University of Birmingham, it comprises of a 150m long track. The track comprises of three sections with the first and last sections used to accelerate and decelerate the train respectively, the middle section is where measurements are collected from using cobra probes. The MMR experiments used an adjusted HST model to account for the firing chassis, 25 runs were completed at a train speed of 40 m/s in order to provide an ensemble average of the data allowing direct comparison to the CFD results.

Computational Domain

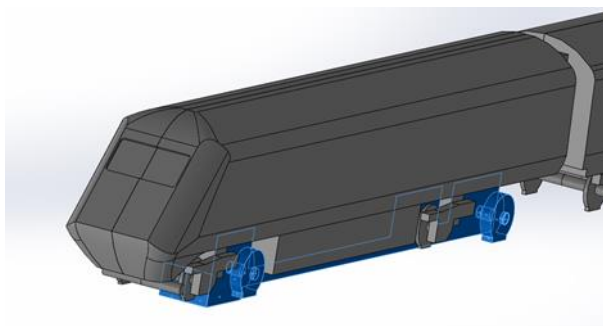


Figure 1: close-up on power car with firing carriage highlighted

A close up of the power car geometry can be seen in Figure 1. The adjustments made to the train's geometry to incorporate the firing chassis used at the MMR can be seen highlighted. These adjustments include larger wheels mounted at a wider gauge to fit the rails at the MMR along with a box section core and a representation of the firing mechanism.

For the computational domain the recommendation made in section 5.3.4 of the British Standards (BSI) [5] is for this blockage ratio to be below 10% in order to achieve accurate results, this recommendation is surpassed by the geometry used in these simulations which has a blockage ratio of 3.4%.

Numerical Details

The OpenFOAM software package [6] was used for conducting the CFD simulations. The initialisation of the CFD simulations was conducted using a potential flow solver, the potentialFoam utility within OpenFOAM. These potential flow simulations were run in order to provide stable initial conditions for the simulations. The DDES approach used the PISO algorithm [7] for the pressure-velocity

coupling. A second order, implicit approach was chosen for the time scheme. A cell limited second order Gaussian integrated central differencing approach was chosen for the gradient schemes. The vector fields used a limited central differencing scheme, the limiter used was the Sweby limiter [8]. To be representative of the moving model rig experiment where it is the train that moves through the air, the floor boundary of the domain was set to move at the free stream velocity of the air (40 m/s). Setting the floor as moving will prevent the build-up of a boundary layer which would lead to inaccuracies. The surfaces of the train were set to a no-slip boundary condition whilst the sides and roof of the computational domain were set to slip conditions. The CFD results were time averaged to allow comparison to the experimental results, this averaging process was started once the turbulence statistics had stabilised and no longer changed with time.

Meshing

The meshes used within this research were produced using the SnappyHexMesh utility within the OpenFOAM software package. A mesh sensitivity study was conducted and found that a mesh of 48 million cells provided the optimum balance between computation time and results accuracy when compared to experimental data. The mesh can be seen in Figure 2. The mesh features 5 Layer cells with the first layer height giving a y^+ value of below 1 using the equation:

$$y^+ = \frac{u_* y}{\nu}$$

Where u_* represents the frictional velocity, y the wall normal distance between the midpoint of the first row of cells and the wall and ν representing the kinematic viscosity.

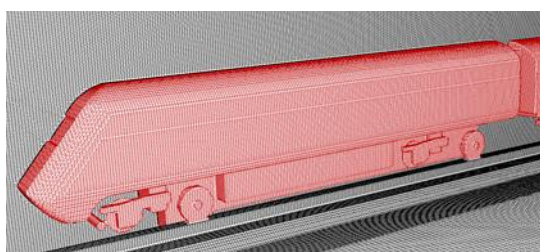


Figure 2: close-up on power car mesh and a central slice through the domain.

Results

The results obtained from the CFD simulations show similar trends along both measurement lines.

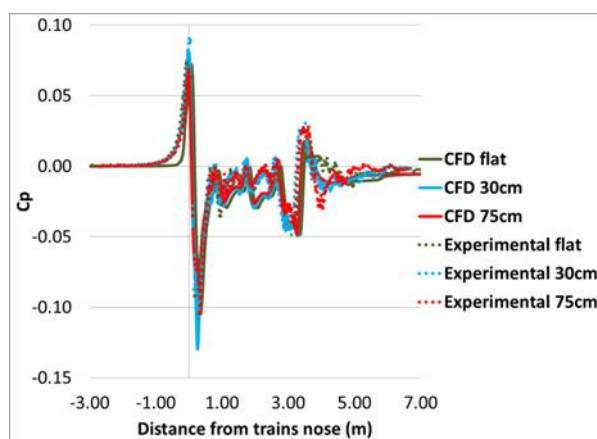


Figure 3: Cp at measurement location A

In figure 3 the results are shown for line A, at this location there is good agreement between the experimental Cp and the CFD results, the initial pressure spike at the train's nose is marginally under predicted by all three CFD approaches. The negative pressure spike just after the train's nose is more closely predicted with only the 30cm CFD results over predicting the pressure drop. Along the sides of the passenger carriages especially the second one all of the CFD results under predict the pressure. For the tail car the pressure results again match up well. Little difference can be seen between any of the results at different ballast shoulder heights. This shows that ballast shoulder height has little to no effect on the slipstream pressures at this location.

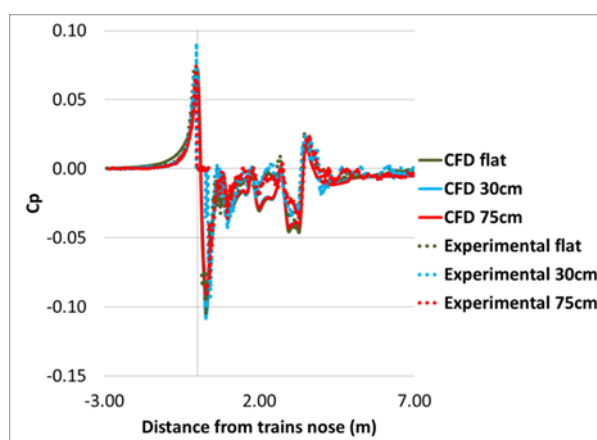


Figure 4: Cp at measurement location B

Figure 4 shows the Cp results for the second measurement location, B. like the results in figure 3 there again is little notable difference in the CFD predicted or experimentally measured pressure coefficients at the different ballast shoulder heights. This suggests that ballast shoulder heights do not have a significant effect on the slipstream pressure profiles along a train. Once again the CFD results under predict the pressure spike at the train's nose, however this time all three simulations over predict the negative pressure spike that follows.

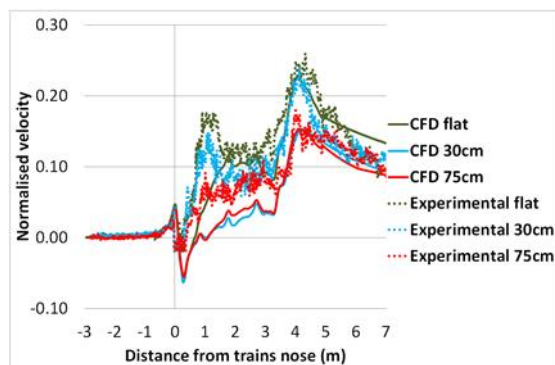


Figure 5: Normalised velocity at measurement location A

Figure 5 shows the normalised velocity profile along measurement line A. At this location large differences between the various ballast shoulder heights can be seen within the experimental data. Within the CFD results the difference is not as clear. There is a large difference between the flat ground cases and the ballast shoulder heights but both the 30cm and 75cm results predict near similar results. The reason these two results are near identical is due to the CFD approach predicting that the flow in both cases will spill down the ballast shoulder, in the 75cm case this ballast shoulder is of course longer so the vortices travel further down away from the train. In the 30cm results the vortices are unable to travel as far down away from the train but instead used the gained momentum from the small ballast shoulder to roll out along the ground from the train. This effect does not occur appear to occur within the experimental results hence the measured difference between all three ballast shoulders. This lack of agreement with experimental results is in part due to a difference in the surface roughness on the embankments.

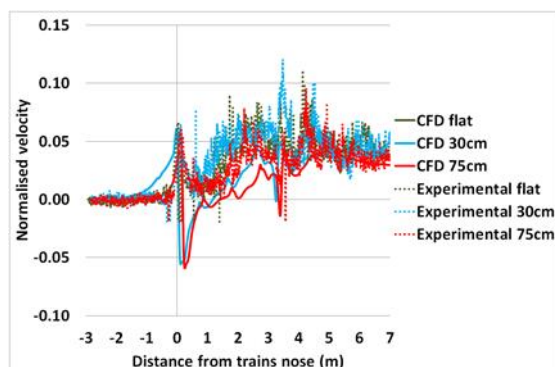


Figure 6: Normalised velocity at measurement location B

Figure 6 shows the normalised velocity profile along measurement line B, at this location the variation in the normalised velocity is significantly less. This reduction in variation is due to the increased height of the measurement location, at this increased height the slipstream is being created mainly by the train body and not the undercarriage region which is most affected by the ballast shoulder. This is also the reason for the decrease in overall normalised slipstream velocity. This reduction in variation also leads to a reduction in the difference between the CFD and experimental results. Though not as noticeable at this location the link between ballast height and the reduction in velocity is still shown, this time between all three CFD simulations. The reason this

location produces different predictions between all three results unlike location A is due to the vortices at this location not being shed down the side of the ballast shoulder like at A but instead being allowed room to expand different amounts down towards the undercarriage space.

Conclusion

The CFD results show good agreement with the experimental data for the C_p . The results for the normalised velocity do not align as well. It can be seen that the CFD results predict little difference between the 30cm and 75cm ballast shoulders due to the slipstream in both cases moving a similar distance away from the train. The CFD results clearly show that ballast shoulder height does have an effect on the slipstream velocities of a train and a reduced effect on the pressures.

Acknowledgement

The computational resources provided by the Birmingham Environment for Academic Research (BlueBEAR) are gratefully acknowledged.

Funding

This work is sponsored by the UK Engineering and Physical Science Research Council (EPSRC) grant number: EP/I03842X/1.

References

- [1] TSI (2008), Commission Decision of 21 February 2008 concerning the technical specification for interoperability relating to the rolling stock subsystem of the trans-European high-speed rail system. Technical report, official Journal of the European Union.
- [2] Spalart, P. R., Deck, S., Shur, M., Squires, K., Strelets, M. K. & Travin, A. 2006. A new version of detached-eddy simulation, resistant to ambiguous grid densities. *Theoretical and computational fluid dynamics*, 20, 181-195.
- [3] Spalart, P & Allmaras, S. 1992. A one-equation turbulence model for aerodynamic flows. 30th Aerospace Sciences Meeting and Exhibit. American Institute of Aeronautics and Astronautics.
- [4] Hemida, H. & Baker, C. The calculation of train slipstreams using large-eddy simulation techniques. *World Congress on Railway Research*, 2011.
- [6] OpenFOAM, 2014: Online: <http://www.openfoam.com> (last visited, 1/10/2014).
- [7] Issa, R. I. 1986. Solution of the implicitly discretised fluid flow equations by operator-splitting. *J. Comput. Phys.*, 62, 40-65
- [8] Sweby, P. 1984. High Resolution Schemes Using Flux Limiters for Hyperbolic Conservation Laws. *SIAM Journal on Numerical Analysis*, 21, 995-1011.
- [5] BSI 2009. EN 14067-4:2005+A1:2009. Part 4: Requirements and test procedures for aerodynamics on open track. BSI

Modularity in gene expression across animal development

Alfredo Rago^{1*}, Jack Werren², John K. Colbourne¹

¹Environmental Genomics group, School of Biosciences, University of Birmingham, UK

²Department of Biology, University of Rochester, Rochester, New York, USA

[*AXR280@bham.ac.uk](mailto:AXR280@bham.ac.uk)

Abstract

What are the units of evolution? From its inception, evolutionary theory focused on individual organisms as the units under natural selection. Yet there is much evidence that selection also acts at lower levels of biological organization, optimizing the functions of individual gene products independently of the whole organism. By contrast, high-throughput gene expression and knock-out studies now demonstrate that virtually every gene requires interactions with products of other genes and external environment to carry out its functions (Mackay & Anholt 2006). If true, the ability of each gene to be selected independently of other genes will be constrained by its need to form stable functional interactions (Papakostas et al. 2014). It is time to break new ground by unifying the dynamics of how genes are co-regulated with those of selection in order to identify the genetically encoded functional modules that are targets for evolution. Current tests of significant changes in gene expression operate under the pan-reductionist framework by detecting changes in mean expression between different conditions for every gene (Soneson & Delorenzi 2013; Smyth 2005). Alternatively, the most common multivariate methods employed in gene expression studies deconvolute gene modules based on their correlation and generate network graphs that display their relative association (Allen et al. 2012) Both approaches present a theoretical hindrance for a biologically meaningful interpretation of their results when applied to gene expression data: Gene-specific linear models do not include explicit tests for gene-gene interactions; machine learning and correlation clustering are unable to discriminate the relative contributions of our conditions of interest to the observed gene-gene correlations. Here, we implement a method for condition-specific detection of gene co-regulation based on cluster modularity. This method relies on a correlation based clustering approach to identify gene-gene interactions and on permutation-based linear models to test for variation of relevant network concepts across experimental conditions. Further to that, I employ this condition-specific network-based framework to provide an interpretation of gene expression patterns in sexual development of the Jewel wasps (*Nasonia vitripennis*) from both a gene regulation and gene evolution perspective.

Data source and quality controls

The data used in this study consists of a developmental time series of transcriptional activity of whole animals in males and females of the jewel wasp *Nasonia vitripennis*. The experimental design comprises five distinct developmental stages from early embryo to sexually mature adult, for both males and females. Each of these conditions was sampled in triplicate. All animals used for data collection come from an inbred strain with minimal amounts of genetic diversity. Further to that, *Nasonia* species have an haplodiploid sex-determination mechanism and lack sex-specific chromosomes. Observed differences in the expression profile of males and females are thus likely to be exclusively caused by differential gene regulation rather than by genetic differences between individuals.

All of the data used was generated through the application of single-channel tiling-path microarrays. Prior to our analyses these data were subject to rigorous quality control and normalization procedures. The signal from each probe was normalized to the 99th quantile of expression from the random Markov probes present on each array, which reflect the intrinsic noise levels on each chip. Further to that, probes were assigned to specific exons according to the latest release of the Official Nasonia Gene Set (OGS2.0, Gilbert and Rago et al., in preparation). After these steps the transcriptional status of our samples is expressed as a count table whose entries represent expression of each exon across every sample. Our data is therefore analogous to those produced via RNA-seq, although expressed as a continuous log transformed signal to noise ratio rather than as a discrete number of read counts or proportion.

Transcript deconvolution

Whereas most studies assess the level of expression at the gene level, this approach has a high chance of producing misleading data as it ignores the additional diversity that is generated at the transcriptomic level. Eukaryotic genes are comprised by a continuous series of intronic and exonic sequences. The former are excised during or shortly after transcription. The latter are retained in the mature mRNA either as protein-coding or as untranslated regions (UTRs). Differential inclusion or exclusion of exons (alternative splicing) is a widespread feature of eukaryotic gene regulation. Transcripts of the same gene comprising different combinations of exons (alternative transcripts or isoforms) can trigger different effects despite constant gene expression at the gene level.

A more biologically meaningful alternative is to quantify expression levels of individual transcripts. While more accurate, this latter approach faces several technical challenges. Transcript-based analyses increase the dimensionality of datasets by an average of 1-2 orders of magnitude as they analyze independently each isoform rather than reducing them to a single gene expression value. Solution: we only study independently the exons that show independent behavior in our experiment. They also require reliable assignment of expression values to individual transcripts. Transcript-specific expression is typically obtained by averaging the signals of transcript-specific exons to match those provided by transcript-specific exons (Trapnell et al. 2010). This implies the ability to trace an a priori distinction between transcript specific and transcript aspecific exons, a task delegated to publicly available gene sets. There is however abundant evidence that even the most complete gene set annotations available are just now approaching completeness (Brown et al. 2014). It is therefore preferable adopt data-specific estimation of constitutive and transcript-specific exons in order to enable the detection of novel alternative splicing events relevant to the design of interest.

In order to address these issues we implemented a modified version of the method proposed by Patrick, Buckley, & Yang (2013). Briefly, we perform hierarchical correlation based clustering of exons within each gene. Strong correlations among exons arise from their coexpression as part of a single transcript. Therefore, every cluster will represent either a transcript or the subset of exons that are present across all isoforms (constitutive exons). Constitutive exon clusters can be distinguished from transcript specific exon clusters from their total expression value. Since constitutive exons are present across all transcripts their average expression levels will be always greater than each other individual cluster.

Correlation based clustering is an intuitive and easily implemented way of generating experiment-specific transcript assignments but its results depend on the threshold chosen as a cutoff for independent expression. Whereas Patrick et al.(2013) justify their choice of an arbitrary threshold by matching with previously published data, we find this solution counterproductive to the goal of detecting experiment-specific splicing events, especially in species which currently lack a comprehensive annotation of their transcriptional diversity.

As such, we developed a gene-by-gene bottom up iterative algorithm choosing as a termination clause the presence of a single cluster whose expression is always ranked first or tied. Our choice of termination criterion is based on the biological observation that the vast majority of genes comprise a core set of exons included in all transcripts (Chen 2013). As constitutive exons are present across all transcripts, their signal will approximate the sum of all alternative transcripts and thus be greater than each one individually. In the special case where only one alternative transcript is present in our sample of interest, constitutive exons will be tied first with the only group of alternative transcripts present in the sample. To respect these assumptions a cluster assignment will have to identify a single exon cluster whose expression level is consistently higher than those of all exon groups or tied with the best ranking one. We can thus interpret our termination criterion as the indication that our clustering method has been able to find a valid group of constitutive exons with the lowest correlation cutoff possible. Other groups of exons are classified as belonging to the same transcripts only if their reciprocal correlations are higher or equal to those observed amongst constitutive exons of their own gene. In the scenario where no alternative isoforms are observed for our gene of interest within our experiment the algorithm will converge to a single cluster comprising all exons (all exons are constitutive).

To further improve the flexibility of our algorithm we also include two biologically interpretable parameters that enable fine-tuning of the sensitivity to robustness tradeoff on the termination clause. The sensitivity used generating rankings can be set to exclude an excessive number of significant digits, which likely represent stochastic variation in gene expression measurements. It is also possible to specify the number of samples in which constitutive exons can violate the termination clause, or expected false negatives.

The final output of our clustering method is a reduced count table, with averaged expression values among highly correlated exons. More importantly, each cluster of exons is representative of either total gene expression (in the case of constitutive exon clusters) or isoform specific expression (in all other cases).

We removed negative values (which fall below the noise threshold) before calculating correlations as they might cause spurious signal during clustering, excluded genes which did not display expression for any exon in any of our samples, allowed one exception to the termination clause and reduced the sensitivity to the first three significant digit of gene expression values.

We were able to assign 76.162 exons (42%) to constitutive clusters and 90.181 (49%) to alternative clusters, which were then reduced to 55.486 clusters of which 18.231 constitutive (33%) and 37.255 alternative (66%). We observed an even split between genes with at least one assigned isoform (11.501) and genes that did not show sign of alternative splicing in our experiment (11.648). Genes with alternative splicing were assigned a median of 3 isoforms, consistently with the highly skewed power-distribution of isoforms per gene reported in other animals.

Network construction and cluster assignment

Measuring the absolute amount of each transcript provides an accurate representation of the cell's transcriptional status but it also restricts our ability to investigate the molecular bases of transcript regulation. An increase in a transcript's level can be achieved either by raising the overall RNA production of its gene or biasing splicing towards a specific isoform. Since these two processes are partially interdependent assessing the degree by which they can be selectively targeted to modulate transcript expression is an interesting biological question, especially since different molecular mechanisms might mediate and regulate different steps of the complex RNA maturation process.

To the authors' knowledge, comparisons between transcript regulation via gene regulation and alteration of alternative splicing has so far not been tackled with an integrative approach. The few studies that address splicing as a focus for network analyses do so through exon specific analyses (Dai et al. 2012; Chen & Zheng 2009) and without reference to the regulation of their parent gene. Exon-based approaches are able to identify clusters of co-spliced exons across the experimental treatments but lack the ability to address the relationships between gene expression and alternative splicing as they focus exclusively on the latter, therefore impeding the detection of cross-regulation between the two processes. Further to that the number of exons within a transcriptome is usually larger than those of observed alternative transcripts and imposes an additional computational load.

A popular approach to disentangle signal from gene expression from alternative splicing is to rely on splicing ratios: the relative abundance of a single transcript (or exon) over the total gene expression level (Monlong et al. 2014). Splicing ratios are a continuous 0-1 bound variables that indicate the degree of alternative splicing irrespective of gene expression levels. Calculating splicing ratios requires the ability to measure both the gene-wide and transcript-specific expression levels. We solve this issue through the application of correlation-based clustering (see previous section), which generates clusters of constitutive and alternative exons. Constitutive exons are included in all isoforms observed in our gene and comprise an unbiased estimator of total RNA production, or gene expression. Clusters of alternative exons represent the subset of RNAs that are allocated specifically to each isoform. We can thus reconstruct splicing ratios by dividing the expression value of each non constitutive cluster by its genes' constitutive cluster.

Due to noise in the experimental measurements, two types of exceptions to the expected distribution are possible. Expression ratios higher than 1 can be caused by the relative increase in the error term that occurs when splicing ratios approach unity, an hypothesis confirmed by manual spot-checking and summary statistics. Consequently, we replace splicing ratios above the unity with 1. Divide by zero errors arise when a non-expressed gene contains a group of isoform-specific exons with sufficient noise to breach the cutoff threshold. As these errors are caused by non-expressed genes, we replace divide by zero values with zeroes. The special case of isoforms comprised exclusively by baseline exons is addressed implicitly as it corresponds to $1 - \sum E_i$, where E_i is the isoform-specific expression ratio for each of the genes' other transcripts.

The final dataset used for our network generation consists of two distinct types of data entries. Gene expression values, which reflect total gene expression, and splicing ratio values, that indicate the allocation of total RNA production to individual transcripts. The overall dimensionality of the dataset is given by the sum of the number of genes measured, plus the number of putative transcripts represented by each splicing ratio, multiplied by the number of samples. comparison of

dimensionality in our networks between gene, isoform, exon, transcript and hybrid network. To further simplify analyses, we replaced values below noise threshold with zeroes and removed 13,370 entries (24%) which showed zero variance and are most likely due to genes and exons whose expression is not observed in our dataset. This resulted in a dataset with a total of 42,116 entries, 23% the size of the total number of exons annotated for the *Nasonia* gene set, and 20% the size of the total gene+exon dataset.

We generated a network comprising all data using the WGCNA R package (Langfelder & Horvath 2008), which performs signed undirected weighted network construction via power-scaled correlation. We employed biweight midclustering correlations to ensure robustness to outliers and selected a power-scaling threshold of 20 after verifying that the generated network was consistent with the expected scale-free topology. Following network construction, we applied hierarchical clustering based on topological dissimilarity to detect groups of coexpressed genes together with co-spliced isoforms. Since our aim is to find condition-specific modules, we maximized the sensitivity of the clustering split parameter and set our minimal cluster size at 20 transcripts. We subsequently collapsed all clusters with a distance of 10% or lower.

Our final output generated a total of 341 clusters, with a median size of 63 genes or isoforms.

Resampling and GLM testing of network parameters

The most common method for characterizing gene clusters is testing the changes of their mean expression levels under different treatments via correlation or linear models. These methods enable characterization of clusters through their expression profile but impede investigation of changes in network structure as they reduce transcriptional complexity to a single value per cluster (mean expression). By contrast network construction methods collapse all available data to produce a single network in which connections between genes are an average of all treatments. Using all available data to construct the network is often the wisest choice, as the increased diversity produces a more accurate separation between functionally distinct clusters. However, it also implies that no further data is available to test the relative effect of different treatments to the observed interactions.

Due to these challenges, the field of transcriptional network comparison is still in its early stages. Most published methods on network comparisons consider gene-gene interactions as the actualization of a constant underlying architecture. As a result the role of the diverse conditions under which different transcriptional interactions and network topologies emerge is often overlooked. An example of this mindset is the tensor-based recurrently dense subnetwork approach (Dai et al. 2012; Li et al. 2011; Yan et al. 2007), which uses diversity only as a means to achieve higher resolution between interacting transcripts. This approach is in contrast with biological data, which highlights that molecular interactions are highly contingent on the environmental parameters. In order for us to understand how this contingency is enacted, we need a method to discriminate treatment-specific changes in network topologies.

To overcome the limitations of network-based approaches we employ bootstrapping to generate multiple networks based on random subsets of the dataset. We record the topological parameters of interest across the permuted networks as well as the type of sample treatments that have been

excluded in each permutation. Finally, we evaluate how removal of specific treatments affects the network parameters of interest through the use of linear models.

The core of our method lies in the resampling strategy applied during bootstrapping, which needs to generate both random and non-random removals of samples in regard to our treatments of interest. In our case, we apply two different resampling strategies to address the presence of stage-specific modules and the presence of sex-specific modules within each stage. In the case of stage-specific modules, we want to exclude possible spurious effects from sex-bias while preserving randomness in regard to stage. As such, we constrain bootstrapping to preserve a 1:1 ratio of male:female samples removed from within each stage and remove a total of 6 samples for each permutation. This creates a series of datasets with a constant number of missing samples and sex ratio, but with a number of removed samples from each stage that varies from 0 to 6 (all of the samples in a single stage). In the case of sex-specific modules within each stage we allow variation of sex ratios removing three samples from each stage in each permutation. This generates a series of datasets in which any single stage lacks 3 samples of varying sex ratio.

Since the main focus of our study is the presence of functional (and therefore evolutionarily) cohesive modules, we record two network parameters for each of the modules identified during global network construction (see previous section). Both parameters are modular variants of network density, or the proportion of observed connections over the total possible ones. The first parameter is the network density of all transcripts within a cluster, or integration coefficient. The second parameter is the network density of transcripts within a cluster with those outside of it, or pleiotropy coefficient. In the biological interpretation, integration reflects the degree by which genes are coregulated under a specific treatment, while pleiotropy the residual interactions with transcripts outside of its own functional module.

As densities, both integration and pleiotropy coefficients are 0-1 bound proportions and can be converted to a normally distributed variable through the application of a logit transformation. We therefore employed generalized linear models (GLMs) with a logit link function and a Gaussian error distribution to analyze the changes in integration and pleiotropy coefficients in relation to our treatments of interest. We further confirmed the appropriateness of distributional assumptions via diagnostic plots.

Our method was able to identify x of the total y modules as having statistically significant changes in the modularity indexes.

Future work

In this paper we demonstrate proof of concept for a method of detecting dynamic changes in topological properties of transcriptional networks. Our method is designed to take advantage of the increasing diversity of transcriptomic studies while reducing their complexity to biologically interpretable units. We took special care to enable flexibility in all steps of data treatment. Sensitivity during exon clustering can be finely tuned depending on data quality. The clustering methods employed can be replaced with user-defined ones or even manually specified cluster assignments. Our method is also able to accommodate for arbitrarily complex questions through appropriate design of the resampling strategy. While its initial application is promising, we still need

to perform adequate quality control steps with benchmarking and synthetic datasets to assess the relative impact of noise, platform-specific and sample-specific challenges.

Bibliography

Allen, J.D. et al., 2012. Comparing statistical methods for constructing large scale gene networks. *PLoS one*, 7(1), p.e29348. Available at: <http://www.pubmedcentral.nih.gov/articlerender.fcgi?artid=3260142&tool=pmcentrez&rendertype=abstract> [Accessed September 19, 2013].

Brown, J.B. et al., 2014. Diversity and dynamics of the Drosophila transcriptome. *Nature*, pp.1–7. Available at: <http://www.nature.com/doi/10.1038/nature12962> [Accessed March 19, 2014].

Chen, F.-C., 2013. Are all of the human exons alternatively spliced? *Briefings in bioinformatics*, 15(4), pp.542–551. Available at: <http://www.ncbi.nlm.nih.gov/pubmed/23640569> [Accessed September 14, 2014].

Chen, L. & Zheng, S., 2009. Studying alternative splicing regulatory networks through partial correlation analysis. *Genome biology*, 10(1), p.R3. Available at: <http://www.pubmedcentral.nih.gov/articlerender.fcgi?artid=2687791&tool=pmcentrez&rendertype=abstract> [Accessed September 11, 2014].

Dai, C. et al., 2012. Integrating many co-splicing networks to reconstruct splicing regulatory modules. *BMC systems biology*, 6 Suppl 1(Suppl 1), p.S17. Available at: <http://www.pubmedcentral.nih.gov/articlerender.fcgi?artid=3403501&tool=pmcentrez&rendertype=abstract> [Accessed September 16, 2014].

Langfelder, P. & Horvath, S., 2008. WGCNA: an R package for weighted correlation network analysis. *BMC bioinformatics*, 9, p.559. Available at: <http://www.pubmedcentral.nih.gov/articlerender.fcgi?artid=2631488&tool=pmcentrez&rendertype=abstract> [Accessed August 6, 2013].

Li, W. et al., 2011. Integrative analysis of many weighted co-expression networks using tensor computation. *PLoS computational biology*, 7(6), p.e1001106. Available at: <http://www.pubmedcentral.nih.gov/articlerender.fcgi?artid=3116899&tool=pmcentrez&rendertype=abstract> [Accessed September 29, 2014].

Mackay, T.F.C. & Anholt, R.R.H., 2006. Of flies and man: Drosophila as a model for human complex traits. *Annual review of genomics and human genetics*, 7, pp.339–67. Available at: <http://www.ncbi.nlm.nih.gov/pubmed/16756480> [Accessed September 7, 2014].

Monlong, J. et al., 2014. Identification of genetic variants associated with alternative splicing using sQTLseeker. *Nature Communications*, 5(May), p.4698. Available at: <http://www.nature.com/doi/10.1038/ncomms5698> [Accessed August 20, 2014].

Papakostas, S. et al., 2014. Gene pleiotropy constrains gene expression changes in fish adapted to different thermal conditions. *Nature communications*, 5(0316), p.4071. Available at: <http://www.ncbi.nlm.nih.gov/pubmed/24892934> [Accessed June 4, 2014].

Patrick, E., Buckley, M. & Yang, Y.H., 2013. Estimation of data-specific constitutive exons with RNA-Seq data. *BMC bioinformatics*, 14, p.31. Available at: <http://www.pubmedcentral.nih.gov/articlerender.fcgi?artid=3656776&tool=pmcentrez&rendertype=abstract>.

Smyth, G.K., 2005. Limma: linear models for microarray data. In R. Gentleman et al., eds. *Bioinformatics and Computational Biology Solutions Using {R} and Bioconductor*. New York: Springer, pp. 397–420.

Soneson, C. & Delorenzi, M., 2013. A comparison of methods for differential expression analysis of RNA-seq data. *BMC bioinformatics*, 14(1), p.91. Available at: <http://www.pubmedcentral.nih.gov/articlerender.fcgi?artid=3608160&tool=pmcentrez&rendertype=abstract> [Accessed May 21, 2013].

Trapnell, C. et al., 2010. Transcript assembly and quantification by RNA-Seq reveals unannotated transcripts and isoform switching during cell differentiation. *Nature biotechnology*, 28(5), pp.511–5. Available at: <http://www.pubmedcentral.nih.gov/articlerender.fcgi?artid=3146043&tool=pmcentrez&rendertype=abstract> [Accessed July 9, 2014].

Yan, X. et al., 2007. A graph-based approach to systematically reconstruct human transcriptional regulatory modules. *Bioinformatics (Oxford, England)*, 23(13), pp.i577–86. Available at: <http://www.ncbi.nlm.nih.gov/pubmed/17646346> [Accessed September 4, 2014].

Posters

	Poster Presenter	Title
P1	Shahad Al-Najjar	On The Error in Mass Transfer in A Stirred Vessel Predicted by Frössling-Type Correlations Based on Particle Settling Velocity
P2	Haider Al-Zayadi	Effected VOIP Service By Means Subjective Method Using MOS in LTE Network
P3	Zainab Al-Sharify	Comparing the Performance of Different Impellers in Mixing Viscoplastic Fluids: CFD, Theory and Experiment
P4	Arash Amini	On-line Condition Monitoring of Railway Wheel-sets
P5	Ryan Brown	Software to automatically quantify in vitro angiogenesis
P6	Michael Clancy	Evaluation of Spatially Resolved Spectroscopy (SRS) in Traumatic Brain Injury (TBI)
P7	Jennifer Cutter	Registration of 3D surface images with pre-operative CT/MRI for use in stereotactic robotic neurosurgery
P8	Samane Faramehr	Aerodynamics of trains in tunnels
P9	Danique Fintelman	Numerical investigation of the flow around a cyclist subjected to crosswinds
P10	Rachel Flight	Semi-automated cell counting in phase contrast images of epithelial monolayers
P11	Michaela Gkantou	Numerical study of the structural response of S460 & S690 beams
P12	Richard Marshall	Investigating the potential for plenoptic imaging of the retina
P13	Justin Morden	Effect of ballast shoulder height on a passenger trains slipstreams and wake
P14	Tony Price	SuSi : A Monte Carlo model of a novel proton CT Scanner using Geant4
P15	Estefania Lopez Quiroga	Operational models for ice crystal formation in highly concentrated systems
P16	Shuai Tian	An improved transverse vibration techniques for enhancing heat transfer and temperature uniformity in viscous fluid flow
P17	Austin Tomlinson	Single Driven Vortex Chain in a Confining Potential
P18	Nina Vyas	Visualizing synthetic dental biofilm on teeth using dual energy micro-CT
P19	Shixuan Wang	Capture abnormal return by SVM

Abstracts

On The Error in Mass Transfer in A Stirred Vessel Predicted by Frössling-Type Correlations Based on Particle Settling Velocity

S. Al-Najjar and M. Barigou

School of Chemical Engineering, University of Birmingham

sa216@bham.ac.uk

Mass transfer coefficients in agitated solid-liquid systems are often estimated from a Frössling-type correlation which depends on the particle slip velocity. In a stirred suspension, the slip velocity will be a function of the hydrodynamic conditions prevailing in the vessel as well as particle size, and will vary from point to point. Attempts to measure it or estimate it on the basis of Kolmogorov's theory have not been successful. In consequence, for such calculations, it has been customary to take the free terminal settling velocity of a solid particle, as a representative of its mean slip velocity but the likely error involved has never been quantified, however. Using experimentally based estimates of local slip velocity obtained in a model solid-liquid system of mechanically suspended glass beads in water, we hereby assess the order of magnitude of the error likely to be incurred when using the particle settling velocity for mass transfer calculations.

The local 3D velocity components of both the solid phase and the liquid phase were measured as a function of spatial position in a stirred vessel, using a technique of **Positron Emission Particle Tracking (PEPT)**. The Lagrangian data were analysed using a MATLAB code to obtain a complete Eulerian description of the two-phase solid-liquid flow including time-averaged estimates of slip velocities of the solid particles.

Three different suspensions were studied under the just-suspended regime: **mono-disperse** of **3 mm** diameter particles, **binary-disperse** of **1** and **3 mm** particles, and **poly-disperse** consisting of five different sizes of particles ranging from **1** to **3 mm**. Experiments were conducted at four different total solid mass concentrations: **5.2 wt%**, **10.6 wt%**, **20 wt%** and **40 wt%**. In the binary and poly-disperse suspensions the different size fractions were mixed in equal proportions. Agitation was effected by a 6-Blade 45° pitched-turbine operating in either up-pumping or down-pumping mode. The azimuthally-averaged error between the local mass transfer coefficient based on the true slip velocity and that based on particle settling velocity was plotted as a 2D map to show variations in the vessel. Azimuthally-averaged radial and axial profiles were also plotted. Results showed that the local mass transfer rate varied considerably throughout the vessel and the use of the settling velocity can lead to extremely large errors in the estimation of the local mass transfer coefficient. The error can exceed 300% and was highest in the impeller region and near the wall. The largest particles were the most affected by the degree of polydispersity of the suspension, and exhibited their largest mass transfer errors in the suspension with five particle size fractions.

Comparing the Performance of Different Impellers in Mixing Viscoplastic Fluids: CFD, Theory and Experiment

Z. Talib, Y. Zhao and M. Barigou
School of Chemical Engineering, University of Birmingham

Abstract

Mechanically agitated vessels are widely used in a wide range of industries such as nuclear, pharmaceuticals, minerals, food processing, household and personal care products. Complex fluids including viscoplastic (yield stress) fluids are frequently encountered in these processes. In the mixing of viscoplastic fluids, the impeller creates a 'cavern' within which liquid is in flow, but in the bulk where the shear stresses are below the apparent yield stress the fluid is stagnant, a phenomenon that can be disastrous for many mixing operations. Such caverns were believed to be well mixed regions, but we recently showed that they are in fact generally poorly mixed. Little work has been done, however, to understand which type of impeller is most effective in mixing such fluids by giving larger and better mixed caverns.

The mixing of a Herschel-Bulkley fluid agitated was studied numerically using Ansys-CFX CFD software. The CFD simulations were validated using photographic imaging where by caverns were visualised using methylene blue dye and measured on digital images taken during mixing of a Carbopol polymer solution. Four different types of impeller were investigated: Rushton turbine (RT), a radial flow impeller, pitch blade turbine (PBT), a mixed flow impeller, A310 hydrofoil impeller which produces axial flow, and the 'elephant ear' (ER) impeller, another type of axial flow impeller which was until recently considered good for the mixing of shear-sensitive fluids such as biological cultures.

Cavern size predicted from CFD predictions showed a good agreement with experimental measurements at low power number; at high power number, however, there is a significant divergence from experiment. At high power number the ER agitator generated the largest caverns, whilst at low power number the A310 agitator formed the largest caverns. Overall, however, the ER impeller was considered to be the most efficient impeller since, for a given power consumption, it also generated a well-mixed cavern compared to the other agitators. Results showed that for the PBT, A310 and ER, the up-pumping mode offered significant advantages over the down-pumping mode.

Finally, a number of mechanistic cavern models were tested and compared with experiment and CFD predictions. The analysis showed that the cylindrical model was more suitable for the RT, PBT and A310 impellers, whereas the toroidal model was more suitable for the ER impeller. Based on the experimental measurements obtained in this study, a modified toroidal model has been formulated for each impeller and a general model which can be used for all these impellers has also been developed.

Keywords: Herschel-Bulkley fluid; CFD; Carbopol; PBT, A310, RT and ER impellers; cavern models.

Effected VOIP Service By Means Subjective Method Using MOS in LTE Network

Haider Al-Zayadi¹, Mushtaq Al-Shuraifi², Talib Al-Sharify³, Zainab Al-Sharify⁴

¹ Iviv Polytechnic National University Institute of Telecommunications, Radio Electronics and Electronic Technics, Ukraine,

² Taras Shevchenko National University of Kyiv, Radio Radio Physics, Electronics and Computer Systems faculty, Ukraine,

³ College of Engineering Sciences, Al-Rafidain University, Hay al-Mustansiryiah, P. O. Box 46036, Baghdad, Iraq

⁴ School of Chemical Engineering, University of Birmingham, UK

Mushtaq_talib2005@yahoo.com

Abstract

With exponential increase in the volumes of video traffic in cellular networks, there is an increasing need for optimizing the quality of voice delivery. 4G networks (Long Term Evolution – Advanced or LTE-A) are being introduced in many countries worldwide, which allow a downlink speed of up to 1 Gbps and uplink of 100 Mbps over a single base station. This makes a strong push towards voice broadcasting over LTE networks, characterizing its performance and developing metrics which can be deployed to provide user feedback of voice quality and feed-back them to network operators to fine-tune the network. In this paper, the performance of voice transmission over LTE-network was characterized and user perceived quality of service for mobile VOIP have been studied in term mean opinion score (MOS) using effected codec for different bandwidth. The simulation results for LTE network show that MOS changed for each codec with 1.4 MHz and 20 MHz, which means when increasing the bit rate according to the type of codec, will lead to an increase MOS in the network.

Keyword: - transfer rate(R), mean opinion score (MOS), voice over ip (VOIP), quality of service (QOS),quality of experience(QOE).

Introduction;

The cellular networks are migrating towards a new technology 4G LTE which is 10x faster than 3G. Boosted bandwidth allows for quicker uploads and better streaming quality. LTE-A targets to achieve peak uplink and downlink data rates of 500 Mbps and 1 Gbps, respectively, for low-speed UEs and around 100 Mbps for those with higher motilities. It accommodates the next generation of telecommunication services such as realtime high-definition. In LTE-A systems, the bandwidths in both uplink and downlink can go up to 100 MHz, which is achieved by Carrier Aggregation (CA) or aggregation of individual Component Carriers. The structure of LTE networks is changed radically from the GSM and UMTS network structures (see figure 1). eNB (Evolved NodeB) is the only node type in EUTRAN (Evolved UTRAN) responsible for all radio interface-related functions. Main node types in the EPC (Evolved Packet Core) are the MME (Mobility Management Entity) responsible for mobility, UE (User Equipment) identity, and security management functions, the S-GW (Serving Gateway) terminating the interface towards E-UTRAN, and the PGW (PDN Gateway) terminates the interface towards the packet data network (PDN).

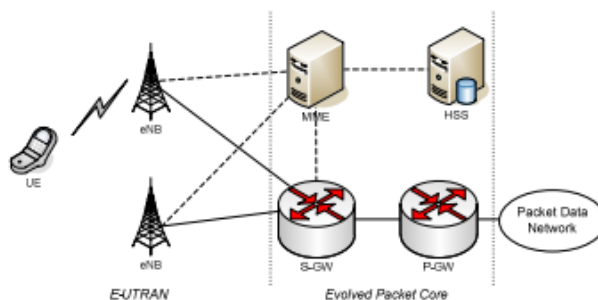


Figure 14 LTE network structure

It should be noted that the circuit switched domain was finally removed from the network architecture. In LTE voice services are not delivered through dedicated nodes in the core network, but through VoIP-based mechanisms in other subsystems like Multimedia Telephony (MMTel) [1] in the IP Multimedia Subsystem [2]. Also, 3GPP decided to define a circuit switched fall back (CS fallback) approach [3] as an intermediate solution. Furthermore, 3GPP also began to study yet another approach, namely circuit-switched over packet switched system (CS over PS). That work was taken over by the VoLGA Forum [4] working on support of voice services over LTE using the GAN (Generic Access Network) standard. This paper presents a comparative study on user-perceived quality of service for Mobile VoIP applications in LTE networks. Results are presented as user-perceived quality of service in terms of Mean Opinion Score (MOS) values for various system bandwidths and codec types. The effect of rating transmission was studied for many parameters such as packet losses and packet delay

Quality of Service (QoS) and

Quality of Experience (QoE)

Internet is a network consisting of different elements such as routers, servers and many nodes which are distributed and connected throughout a geographical area. The service delivery of Internet is based on best effort model which treats the traffic equally regardless of the nature of the traffic which can be delay, packet lost or rate sensitive. As the number of user's increases the Internet develops more and more, the concept of quality of service has been widely discussed. QoS consists of some network performance metrics, which differentiate the Internet flows. Quality of Experience (QoE) is a customer satisfaction of network services. Therefore, performance metrics in QoS parameters like, rate, packet loss, latency and jitter effect on the user's QoE are important. Different applications have different set of requirements for network parameters such as delay, jitter, packet loss and bandwidth, e.g., real time applications such as VoIP are more sensitive to delay. On the other hand, non-real time applications such as web browsing can tolerate some delay but are sensitive to packet loss. Quality of Service is the ability of the network to provide some flows with their specific needs. Thus, QoS requires supporting dedicated bandwidth, improving loss characteristics, avoiding and managing network congestion and shaping and prioritizing the flow traffic.

On the other hand, Quality of Experience (QoE) provides a way of quantifying how subscribers perceive the offered applications. It provides some means to measure overall customer satisfaction of a service and hence, of assessing the improvement techniques that can be implemented when

needed. QoE can mean different things for different applications. For example, an audio application may get a high QoE based on sound fidelity whereas a high QoE is related to a large and clear picture for a video application. In order to maintain quality of experience, different algorithms are proposed to do policing, scheduling, labeling and many other tasks to satisfy a certain thresholds of QoS metrics during a communication session. These QoS-based approaches cannot completely describe and satisfy user's perception quality which encourages us to derive a QoE description method based on network parameters.

QoS classes

When defining the IMT-2000 QoS classes the restrictions and limitations of the radio interface have to be taken into account. The QoS mechanisms provided in the IMT- 2000 network have to be robust and capable of providing reasonable QoS resolution. Table 1 illustrates proposed QoS classes for IMT-2000. In the proposal there are four different QoS classes (or traffic classes) [5]:

- Conversational class
- Streaming class
- Interactive class
- Background class.

The main distinguishing factor between these classes is how delay sensitive affect the traffic. The conversational class is meant for traffic which is very delay sensitive while background class is the most delay insensitive traffic class. Conversational and streaming classes are mainly intended to be used to carry realtime traffic flows. The main divider between them is how delay sensitive the traffic is. Conversational real-time services, like video telephony, are the most delay sensitive applications and those data streams should be carried in conversational class. Interactive class and background are mainly meant to be used by traditional Internet applications like WWW, e-mail, Telnet, FTP and news. Due to loosing delay requirements, compared to conversational and streaming classes, both provide better error rate by means of channel coding and retransmission. The main difference between interactive and background class is that interactive class is mainly used by interactive applications, e.g. interactive e-mail or interactive Web browsing, while background class is meant for background traffic, e.g. background download of emails or background file downloading. Responsiveness of the interactive applications is ensured by separating interactive and background applications. Traffic in the interactive class has higher priority in scheduling than background class traffic, so background applications use transmission resources only when interactive applications do not need them. This is very important in a wireless environment where the bandwidth is low compared to fixed networks.

However, these are only typical examples of usage of the traffic classes. There is in particular no strict one-to-one mapping between classes of service and the traffic classes defined above. For instance, a service interactive by nature can very well use the Conversational traffic class if the application or the user has tight requirements on delay.

Table 1 QoS classes for IMT-2000

Traffic class	Conversational class Real-time conversation	Streaming class Real-time streaming	Interactive class Interactive best effort	Background class Background best effort
Fundamentals characteristics	<ul style="list-style-type: none"> – Preserve time relation (variation) between information entities of the stream – Conversational pattern (stringent and low delay) 	<ul style="list-style-type: none"> – Preserve time relation (variation) between information entities of the stream 	<ul style="list-style-type: none"> – Request response pattern – Preserve payload content 	<ul style="list-style-type: none"> – Destination is not expecting the data within a certain time – Preserve payload content
Example of the application	<ul style="list-style-type: none"> – Voice 	<ul style="list-style-type: none"> – Streaming video 	<ul style="list-style-type: none"> – Web browsing 	<ul style="list-style-type: none"> – Background download of e-mails

Conversational class

The most well-known use of this scheme is telephony speech. But with Internet and multimedia a number of new applications will require this scheme, for example VoIP and videoconferencing tools. Real-time conversation is always performed between peers (or groups) of live (human) end-users. This is the only scheme where the required characteristics are strictly given by human perception. The real-time conversation scheme is characterized by the transfer time that must be low because of:

- The conversational nature of the scheme.
- At the same time the time relation (variation) between information entities of the stream must be preserved in the same way as for real-time streams.

The maximum transfer delay is given by the human perception of video and audio conversation. Therefore the limit for acceptable transfer delay is very strict, as failure to provide low enough transfer delay will result in unacceptable lack of quality. The transfer delay requirement is therefore both significantly lower and more stringent than the round trip delay of the interactive traffic case. The Real-time conversation – fundamental characteristics for QoS are:

- Preserve time relation (variation) between information entities of the stream.
- Conversational pattern (stringent and low delay).

Streaming class

When the user is looking at (listening to) real-time video (audio) the scheme of realtime streams applies. The real-time data flow is always aiming at a live (human) destination. It is a one-way transport. This scheme is one of the newcomers in data communication, raising a number of new requirements in both telecommunication and data communication systems. It is characterized by the time relations (variation) between information entities (i.e. samples, packets) within a flow which must be preserved, although it does not have any requirements on low transfer delay. The delay variation of the end-to-end flow must be limited, to preserve the time relation (variation) between information entities of the stream. But as the stream normally is time aligned at the receiving end (in the user equipment), the highest acceptable delay variation over the transmission

media is given by the capability of the time alignment function of the application. Acceptable delay variation is thus much greater than the delay variation given by the limits of human perception. The Real-time streams – fundamental characteristics for QoS are:

- Preserve time relation (variation) between information entities of the stream.

Interactive class

When the end-user, that is either a machine or a human, is online requesting data from remote equipment (e.g. a server), this scheme applies. Examples of human interaction with the remote equipment are: Web browsing, database retrieval, server access. Examples of machines interaction with remote equipment are: polling for measurement records and automatic database enquiries (tele-machines). Interactive traffic is the other classical data communication scheme that on an overall level is characterized by the request response pattern of the end-user. At the message destination there is an entity expecting the message (response) within a certain time. Round trip delay time is therefore one of the key attributes. Another characteristic is that the content of the packets must be transparently transferred (with low BER). The Interactive traffic – fundamental characteristics for QoS [5] are:

- Request response pattern;
- Preserve payload content.

Background class

When the end-user, that typically is a computer, sends and receives data-files in the background, this scheme applies. Examples are background delivery of e-mails, SMS, download of databases and reception of measurement records. Background traffic is one of the classical data communication schemes where an overall level is characterized by the absence of any parameter at the destination expecting to receive the data within a certain time limit. The scheme is thus more or less delivery time insensitive. Another characteristic is that the content of the packets must be transparently transferred (with low BER). The Background traffic – fundamental characteristics for QoS[5] are:

- The destination is not expecting the data within a certain time;
- Preserve payload content.

In the next section we will discuss the Quality assessment approaches which how to measure and predict Quality experience of a user from a delivered service.

Quality Assessment Approaches

Quality assessment approaches are divided into two main categories: Subjective and Objective. In Subjective methods, surveyed people are asked to grade a perceived service. Objective methods are mathematical models used to approximate results of subjective quality assessment and are further divided into intrusive and non-intrusive methods. Intrusive methods need a reference data and thus, although more accurate, are not suitable for monitoring real time traffic [6]. Depending on the type of application used, there are several objective approaches for assessing the perceived quality. some examples of such approaches are E-model introduced in ITU-T Recommendation G.107 [7] for VoIP which the purpose for our paper application, MSE and PSNR for Video application, G-model for

online game [8] and ITU-T Recommendation G.1030 [9] for web-browsing application. All such objective approaches map user perception of a specific application to network parameters such as delay, jitter and packet loss. In the next section we elaborate on subjective and objective approaches that are more commonly used in literature for MOS & VOIP application respectively.

Subjective Quality Assessment Approach-Mean Opinion Score (MOS)

A well-know QoE metric is Mean Opinion Score (MOS), which quantifies the perception quality of different user-based applications (e.g. Video, VoIP, Gaming and web-browsing). In the MOS method, which is a subjective method of assessing perceived quality of service, there are five categories for evaluating the service. Surveyed people assign a number from 1 to 5 based on service as shown in Table 2:

Table 2: Description of MOS value

MOS Value	Service Quality
1	Unsatisfactory
2	Poor
3	Fair
4	Good
5	Excellent

Subjective methods are expensive and complex to conduct and in many situations are not affordable. Therefore, in order to estimate the quality of impression of human, objective metrics have been developed.

Objective Quality Assessment Approaches in VoIP

Application VoIP has an increasing widespread popularity and is used as alternative to traditional telephony. This popularity can be due to its running over a data network (usually TCP/IP), ease of service expansion/integration and low costs. VoIP protocols consist of H.323, SIP, MGCP and others. Skype and IAX2 are also other less commonly used standards or specific applications. IAX2 is a popular protocol widely used on an Open source platform called Asterisk. There are different methods for implementing VoIP one of these methods is E-model which is an objective method.

Related work

Paisal [10] also qualitatively compared various techniques for delivering VoIP services in LTE networks including CS Fallback, IMS Telephony with handover to CS domain (SRVCC), and Voice over LTE via Generic Access (VoLGA). Paisal concluded CS Fallback and/or VoLGA would be of most interest to operators not intending to deploy IMS. Operators having 2G/3G networks and planning to deploy IMS could consider CS fallback or VoLGA as an intermediate step, but use SRVCC later when IMS has been installed. Those operators deploying IMS together with LTE should go for SRVCC directly, Paisal argued. Puttonen et al. [11] quantitatively studied VoIP performance in LTE downlink (DL) using the Adaptive Multi-Rate (AMR) [12] 12.2 codec in four simulation cases standardized by

3GPP. Maximum capacity was reported to be 60 and 300 UEs per cell at 1.25 MHz and 5 MHz system bandwidth respectively. Henttonen et al. [13] studied the effects of using robust header compression (ROHC) techniques in LTE networks in highly mobile scenarios for VoIP applications. Capacity loss from highly mobile (120 km/h) scenarios was reported to reach 65% compared to near-stationary (3 km/h) scenarios. Our previous work includes a study on user-perceived quality of service for multimedia applications in wireless heterogeneous networks [14]. Furthermore, a study on session setup delay and jitter for a Voice over WLAN (VoWLAN) application was done using composite metrics [15]. Finally, an access network selection mechanism for mobile nodes in a combined WLAN/LTE environment was proposed and evaluated [16].

Mathematical expression

E-model in a first step is a transmission rating factor R , which combines all transmission parameters relevant for the considered connection. This rating factor R is composed of [17]:

$$R = R_o - I_s - I_d - I_{e-eff} + A \quad (1)$$

Where

R_o Represents in principle the basic signal-to-noise ratio

I_s is a combination of all impairments which occur more or less simultaneously with the voice signal

I_d represents the impairments caused by delay

I_{e-eff} represents impairments caused by low bit-rate codecs.

A allows for compensation of impairment factors

To gate R we must calculate R_o , I_s , I_{e-eff} and A the parameters as default value appear in table 3 below

$$R_o = 15 - 1.5(SLR + No) \quad (2)$$

$$I_s = I_{olr} + I_{st} + I_q \quad (3)$$

$$I_d = I_{dte} + I_{dle} + I_{dd} \quad (4)$$

$$I_{e-eff} = I_e + (95 - I_e) \cdot \frac{Ppl}{\frac{Ppl}{BurstR} + Bpl} \quad (5)$$

All parameters above clear in table 3

Parameters	Default value
SLR(Send loudness rating)	8 db
No (Noise Floor)	-64dbmp
I_{olr} (decrease in quality caused by too-low values of OLR)	0.440281 db
I_{st} (impairment caused by non-optimum sidetone)	0.001099
I_q (impairment caused by quantizing distortion)	0.974105
I_{dte} (estimate for the impairments due to talker echo)	0
I_{dle} (impairments due to listener echo)	0.149046
I_{dd} (impairment caused by too-long absolute delay Ta)	0
I_e (Equipment impairment factor)	0
Ppl (Random packet-loss probability)	0%
Bpl (Packet-loss robustness factor)	4.3
BurstR (Burst ratio)	1

We can see or represent all parameters above from figure 2 below according to E-model

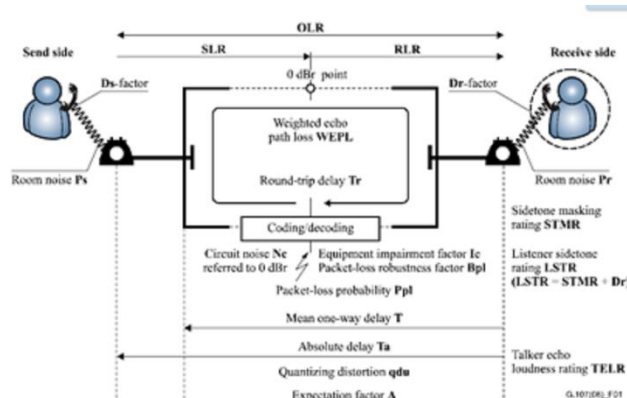


Figure 15 Reference connection of the E-model

Quality measures derived from the transmission rating factor R

The transmission rating factor R can lie in the range from 0 to 100, where $R = 0$ represents an extremely bad quality and $R = 100$ represents a very high quality. The E-model provides a statistical estimation of quality measures. The percentages for a judgment good or better (GoB) or poor or worse (PoW) are obtained from the R -factor by means of the Gaussian error function [18].

$$E(x) = \frac{1}{\sqrt{2\pi}} \int_{-\infty}^x e^{-\frac{t^2}{2}} dt \quad (6)$$

The equations are:

$$GoB = 100E\left(\frac{R-60}{16}\right)\% \quad (7)$$

$$PoW = 100E\left(\frac{45-R}{16}\right)\% \quad (8)$$

As we talk before estimated mean opinion score (MOS) for the conversational situation in the scale 1-5 can be obtained from the R -factor using the equations:

$$MOS = \begin{cases} 1 & \text{for } R < 0 \\ 1 + 0.035 \cdot R + R(R - 60) \cdot (100 - R) \cdot 7 \cdot 10^{-6} & \text{for } R \in [0, 100] \\ 4.5 & \text{for } R > 100 \end{cases} \quad (9)$$

SIMULATIONS AND RESULT

Perceptual Evaluation of Speech Quality (PESQ) is an objective method to assess VoIP quality and is defined in ITU-T P.862. It is one of the most commonly used intrusive method of assessing VoIP quality which uses the non-degraded signal as reference [19]. In order to directly monitor/assess voice quality non-intrusive techniques are used that do not require reference signal. Such techniques either use the degraded signal (e.g., E-model) or the network parameters (e.g., delay, jitter, packet loss, codec ...) [20]. E-model is used which is an objective method and uses impairment factors to calculate R-score which ranges from 0 to 100 [17] and reflects the overall conversational quality as

we talk before. (NB) E-model describes a separate WB-version, it uses similar concepts and input parameters as the E-model. The current version captures the effects of loudness loss, background noise at the sending side, circuit noise, talker echo, absolute delay, wideband speech coding, and voice-over-IP packet loss. The mean rating, averaged over all test participants and stimuli reflecting the same circuit condition, is then called a mean opinion score (MOS). It is an average S-shaped relationship defined between the *R*-scale (range [0;100]) and MOS ratings (range [1;4.5]) collected from "average" test participants in an "average" experimental setting. Using equation 9 above we will get;

$$R = R_o - I_s - I_d - I_{e-eff} \quad (10)$$

Using standard model mathematical for ITE-T 107 we can get the same result which can be represented in figure 3 below;

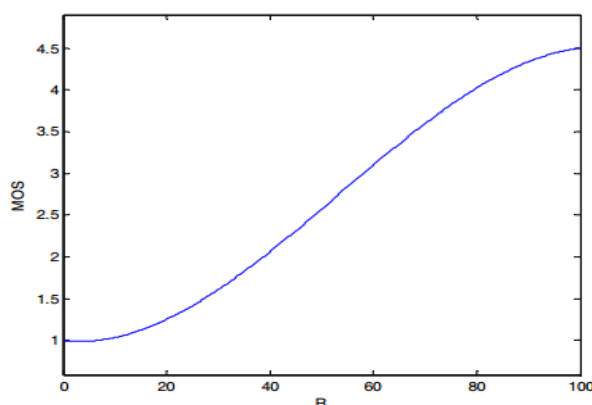


Figure 16 Relationship between MOS values and R values

And we can see from default parameters in this model that the Rating transfer is 93.2 but if any of the parameters is changed, for example a change in packet delay, we will see that the rating transfer became 83.3 this will affect the network performance which lead to a bad quality in service mean voice quality and lead to change in MOS [17]. In this model we show that codec is constant in figures 4 and 5. The resulted parameters are shown in tables 4 and 5. We must observe these values for E-model when we have in the network two users one transmitting and one receiving. But when more than one user are transmitting and receiving in the same time, which clearly in our simulation below, this will lead to effect MOS in the network, according on our result below this means that the number of users represent the first parameter and codec second parameter effect on MOS for network.

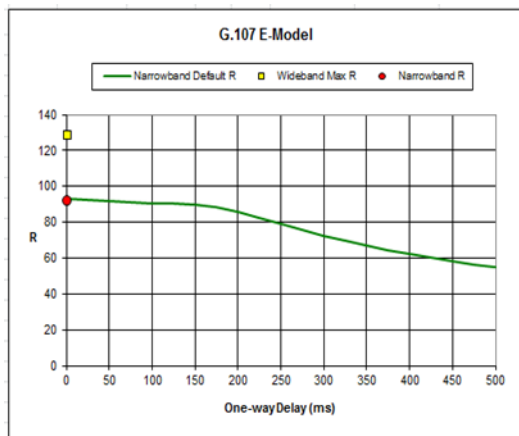


Figure 17 Rating transfer 93.2 for SLR=8

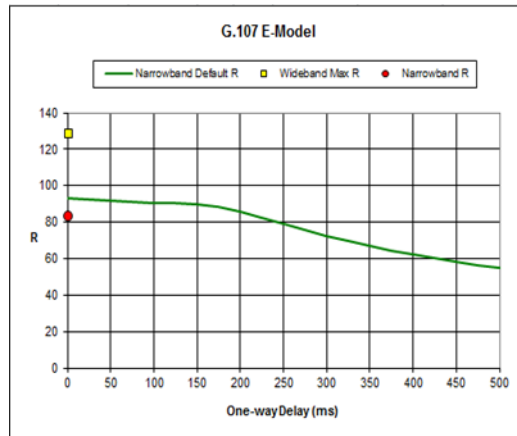


Figure 18 Rating transfer 83.3 for SLR=15

Table 4 Delay impairment factor alter change in SLR =15 rating transfer=93.2

Delay impairment factor	Value
I_d	0.147703
I_{dte}	0
I_{dtes}	0.001099
I_{dle}	147703
I_{dd}	0
X	0
MOS	4.409421

Table 5 Delay impairment factor alter change in SLR =15 & rating transfer=83.3

Delay impairment factor	Value
I_d	0.149046
I_{dte}	0
I_{dtes}	0.001099
I_{dle}	0.149046
I_{dd}	0
X	0
MOS	4.143209

Our simulation clear in figure 6 below which used four cells with three UEs per cell were configured, so that each UE started a phone VoIP call to any other randomly selected UE. Here we used FDD mode because we can control on bandwidth so we postulate that uplink frequency 19200 MHz and downlink frequency 2110 MHz and used short normal cyclic prefix not extended cyclic prefix per slot.

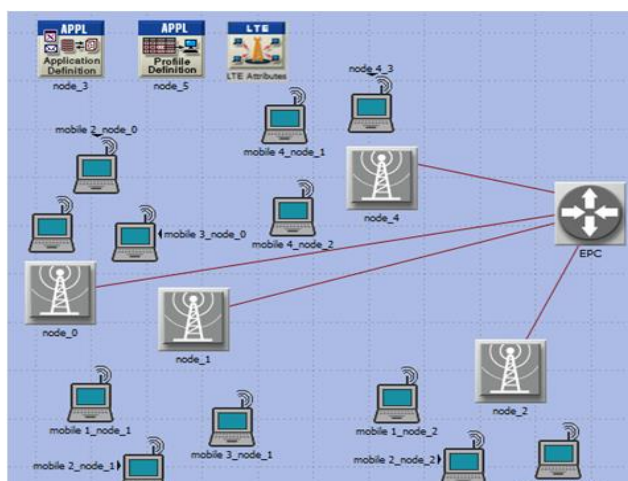


Figure 19 simulation design

Here study affected codec on MOS by used OPNET Modeler 16 simulation for different bandwidth NB and WB. After simulating VoIP traffic in the LTE network, we got results according to Table 6.

Table 6 Simulation Results (MOS values)

VoIP Codec	System Bandwidth	
	(MOS) in 1.4 MHz	(MOS) in 20 MHz
GSM FR	2.51	3.49
G.729 A	3.02	3.03
G.723.1 5.3K	2.51	2.51
G.711	3.64	4.64

Obviously, using high bitrate codecs (the G.711 with a nominal bitrate of 64 kb/s) gives higher MOS values. The other more low-bitrate codecs (GSM FR, G.723.1 5.3K, and G.729 A) give lower MOS values. The GSM FR codec, however, performs quite well in the 20 MHz system bandwidth scenario.

Conclusion

Voice services in LTE are still being defined and standardized. Today, mobile broadband is the predominant service delivered in commercial LTE networks. Voice being a very important feature in all telecommunication networks and also the main revenue source for operators makes standardization of voice services in LTE which is a very important issue. And we see after changing SLR from 8 to 15 a change in R from 93.2 as default to 83.3, and MOS changes from 4.409421 to 4.143209 respectively. This effect the network therefor if we want good quality in voice we must raise the rating transfer and minimize the delay in signal, which represents one of the parameters that we work on it from E-model. From our simulation we can see that the result for LTE network the MOS change according to the change for each codec with 1.4 MHz and 20 MHz This means that when we increase the bit rate of according type of codec will lead to an increase in the MOS of the network.

References

- [1] 3GPP TS 22.173, IP Multimedia Core Network Subsystem (IMS) Multimedia Telephony Service and supplementary services, Stage 1. September 2009.
- [2] 3GPP TS 23.228, IP Multimedia Subsystem (IMS), Stage 2. March 2010.
- [3] 3GPP TS 23.272, Circuit Switched (CS) fallback in Evolved Packet System (EPS), Stage 2. June 2011.
- [4] VoLGA Forum. Available at www.volga-forum.com. Accessed on August 4, 2011.
- [5] 3GPP TSG-SA #17 Proposed contribution to ITU-R WP8F on the Revision of Recommendation ITU-R M.1079 Biarritz, France, 9th – 12th September 2002
- [6] W. M. Eddy. At what layer does mobility belong. IEEE Communications Magazine, 42(10):155 – 159, 2004.
- [7] G.107 ITU-T. The E-Model, A Computation Model for Use in Transmission Planning, 2005.
- [8] D. Picovici et. al. Subjective-based quality assessment for online games. 3rd International ICST Conference on Simulation Tools and Techniques, 2010.
- [9] ITU-R Recommendation G.1030. Estimating end-to-end performance in IP networks for data applications, 10 2005.
- [10] V. Paisal. Seamless Voice over LTE. In Proceedings of 4th IEEE Conference on Internet Multimedia Services Architecture and Application (IMSAA 2010), Bangalore, India, December 15–17, 2010.

[11] J. Puttonen, T. Henttonen, N. Kolehmainen, K. Aschan, M. Moio, and P. Kela. Voice-Over-IP Performance in UTRA Long Term Evolution Downlink. In Proceedings of the 2008 IEEE 67th Vehicular Technology Conference (VTC-Spring 2008), Singapore, May 11–14, 2008.

[12] 3GPP TS 26.093, Mandatory speech codec speech processing functions, Adaptive Multi-Rate (AMR) speech codec, Source controlled rate operation, Release 10. March 2011.

[13] T. Henttonen, K. Aschan, J. Puttonen, N. Kolehmainen, P. Kela, M. Moio, and J. Ojala. Performance of VoIP with Mobility in UTRA Long Term Evolution. In Proceedings of the 2008 IEEE 67th Vehicular Technology Conference (VTC-Spring 2008), Singapore, May 11–14, 2008.

[14] K. Andersson, D. Granlund, and C. Åhlund. M4: Multimedia mobility manager: a seamless mobility management architecture supporting multimedia applications. In Proceedings of the 6th International Conference on Mobile and Ubiquitous Multimedia (MUM '07), Oulu, Finland, December 12–14, 2007.

[15] M. Elkotob and K. Andersson. Analysis and measurement of session setup delay and jitter in VoWLAN using composite metrics. In Proceedings of the 7th International Conference on Mobile and Ubiquitous Multimedia (MUM '08), Umeå, Sweden, December 3–5, 2008.

[16] K. Andersson and C. Åhlund. Optimized Access Network Selection in a Combined WLAN/LTE Environment. To appear in Wireless Personal Communications, Fall 2011.

[17] G.113 ITU-T. Transmission impairments due to speech processing, 11 2007.

[18] ITU-T G.107 Telecommunication standardization sector of ITU (12/2011)

[19] G.109 ITU-T. Definition of categories of speech transmission quality, 09 1999.

[20] S. Winkler. Digital video Quality: Vision Models and Metrics. John Wiley and Sons Publication, 2005.

Online Condition Monitoring of Railway Wheelsets

Arash Amini¹, Dr Mayorkinos Papaelias¹ and Prof Clive Roberts

School of Electronics, Electrical and Computer Engineering, University of Birmingham, B15 2TT

axa194@bham.ac.uk

Abstract

Typical railway wheelsets consist of three main components; the wheels, axle and axle bearings. Wheelset failures are not uncommon and occur unexpectedly. Faults can develop on any of the aforementioned components, but the most common are related to wheel and axle bearings defects. The rail industry has focused on the improvement of maintenance and online condition monitoring of rolling stock to reduce the probability of failure as much as possible. This paper discusses the development of a novel methodology based on the application of acoustic emission in order to detect wheel and axle bearing defects at an early stage before they result in final failure. A set of onboard and wayside experiments have been conducted on actual rolling stock with artificially induced faults on a number of axle bearings. Acoustic emission sensors were mounted on the bearing case and on the rail for the onboard and wayside measurement respectively. The results obtained prove that the acoustic emission method is capable of identifying wheel and axle bearing faults successfully both onboard and wayside. Various signal processing techniques based on moving RMS, moving kurtosis filtering, and spectral analysis have been used in order to process the acoustic emission data acquired.

Software to automatically quantify morphological features in an angiogenesis assay

Ryan M. Brown¹, Christopher J. Meah¹, Victoria L. Heath², Roy Bicknell² and Iain B. Styles³

¹PSIBS DTC, Chemistry West, University of Birmingham, UK.

²Institute of Biomedical Research, College of Medical and Dental Sciences, University of Birmingham, UK. ³School of Computer Science, University of Birmingham, UK.

rxb870@bham.ac.uk

Angiogenesis involves the generation of new blood vessels from the existing vasculature and is dependent on many signalling pathways^{1,2}. *In vivo* angiogenesis is dynamic and complex, meaning assays are commonly utilised to explore specific targets for research into this area.² Tube forming assays are widely used to characterise these processes, the matrigel tube forming assay is a simple to implement but powerful tool in identifying biomolecules involved in angiogenesis³. Images are

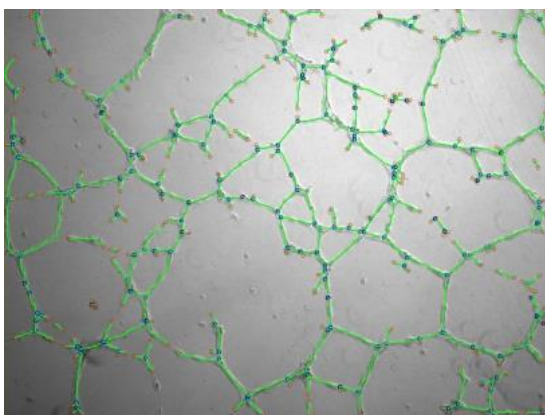


Figure 20: Phase contrast image of a HUVECs network formed during the matrigel assay, overlaid with resulting morphological operations performed in post-processing.

acquired during the assay, as the HUVECs migrate into network-like structures (Figure 1), dependent on stimulating factors such as VEGF. The images of the endothelial network then require manual quantification of morphological parameters by the user, leading to observational bias and user subjectivity². Herein, we present a program designed to quantify common morphological features in the images, requiring limited user-input. Morphological image-processing successfully segmented the HUVECs network and rapidly quantified features such as nodes, branch length and loops; removing user subjectivity and bias. Automation of the

analysis allows high throughput studies to be undertaken, which is essential in screening anti- and pro-angiogenic factors, in the development of novel anti-cancer targets². The program is currently being produced into an ImageJ plugin, as an open-source platform for angiogenesis researchers, to coincide with the release of an angiogenesis protocols book.

References

- [1] Adams, R. H. & Alitalo, K. 2007. Molecular regulation of angiogenesis and lymphangiogenesis. *Nat. Rev. Mol. Cell Biol.* **8**, 464–78.
- [2] Heath, V. L. & Bicknell, R. Anticancer strategies involving the vasculature. 2009. *Nat. Rev. Clin. Oncol.* **6**, 395–404.
- [3] Auerbach, R., Lewis, R., Shinnars, B., Kubai, L. & Akhtar, N. 2003. Angiogenesis assays: a critical overview. *Clin. Chem.* **49**, 32–40.

Evaluation of Spatial Resolved Spectroscopy (SRS) for use in monitoring Traumatic Brain Injury (TBI) patients

Michael Clancy¹, Anthony Belli², David Davies², Zhangjie Su², Samuel Lucas³ and Hamid Dehghani¹

¹ School of Computer Science, ² Clinical and Experimental Medicine, ³ School of Sport, Exercise and Rehabilitation Science, University of Birmingham, UK

mxc933@bham.ac.uk

Spatial resolved spectroscopy (SRS) obtains a relative measure of deep tissue oxygenation, in a variety of contexts, by analysing the slope of detected light that is attenuated over a series of multi-distance detectors [1]. In principle this technique provides a means of assessing cerebral oxygenation, while minimizing the signal contributions from superficial layers (scalp and skull); this is currently a limiting factor in functional near infrared spectroscopy (fNIRS) systems [2]. In brain injury the cerebral dynamics do not mirror that of the superficial layers, hence, it is paramount to obtain deep tissue signals. The aim of this investigation was to assess the validity of SRS for TBI monitoring through finite element model (FEM) simulations on a realistic 5-layered 3D head mesh.

Calculated TOI changes using Niro-200NX geometry for known brain SO₂ values

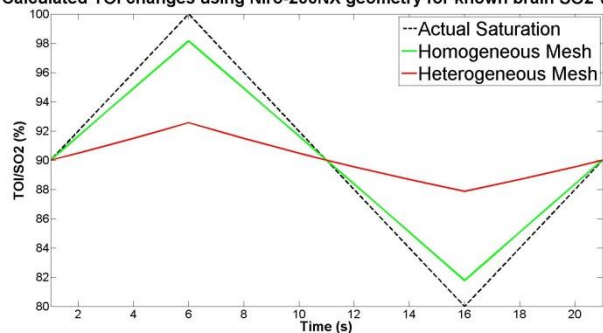


Figure 1 – Calculated TOI values when brain saturation was varied between 80 and 100%.

Effects of scatter and superficial absorption changes on TOI range

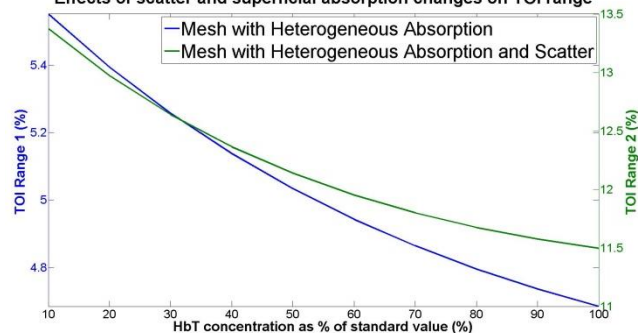


Figure 2 – Sensitivity of SRS to cerebral saturation when superficial HbT levels are varied.

Simulations demonstrated that SRS was valid for a homogeneous mesh (Fig. 1). Specifically, when brain saturation was changed by 20% the tissue oxygenation index (TOI) changed by 16.4%. With a heterogeneous mesh however, the total TOI change was only 4.7%. This finding indicates that superficial layers obscured the deep tissue signals. When the absorption in the superficial layers was decreased, by lowering total haemoglobin (HbT) concentration (Fig. 2), the TOI range showed an increased accuracy of ~19% (for a 90% reduction in HbT); albeit still 72% lower than expected. Repeating the simulations with homogeneous scattering properties showed that SRS is also strongly affected by heterogeneous scatter conditions (Fig. 2). This illustrates that, while SRS samples the correct depth and is limited by superficial signals, assumptions regarding scatter are the main source of inaccuracy. To improve upon this, we plan to develop and test a hybrid fNIRS/DOT probe and reconstruction algorithm. We propose that, instead of bypassing or subtracting out superficial changes and scatter, reconstruction of all parameters will give a true spatially resolved model.

Acknowledgements: This work has been funded by the Engineering and Physical Sciences Research Council (EPSRC). The FEM code is distributed as part of the NIRFAST modeling software at <http://www.nirfast.org>.

References

1. Suzuki, S., et al. Tissue oxygenation monitor using NIR spatially resolved spectroscopy. in BiOS'99 International Biomedical Optics Symposium. 1999. International Society for Optics and Photonics.
2. Ghosh, A., C. Elwell, and M. Smith, Cerebral near-infrared spectroscopy in adults: A work in progress. *Anesthesia & Analgesia*, 2012. 115(6): p. 1373-1383.

Aerodynamics of trains in tunnels

S. Faramehr¹ and H. Hemida²

¹School of Civil Engineering, University of Birmingham, UK.

²School of Civil Engineering, University of Birmingham, UK.

SXF192@bham.ac.uk

When a train moves through air, it generates a turbulent flow around it called a slipstream. The slipstream is associated with high air velocities and rapidly-changing pressure fields. These aerodynamic issues are still valid when a train passes a tunnel and in addition to these, the compressibility of the air around high-speed trains produces what are called “micro-pressure waves” as a result of running in a confined space. The air velocity, pressure variation and direction of the flow inside tunnels is different to the slipstream in open air. These differences depend on the size of the tunnel (cross section and length of the tunnel) and the shape and speed of the train.

In the present thesis, the effect of tunnel length on the flow and pressure inside is investigated. The investigation uses computational fluid dynamics techniques (CFD), in which a 1/25th model of the ICE2 train is used. Two tunnel lengths are investigated; one is double the length of the other. The sliding technique is employed to simulate the movement of the train in the tunnel. The simulation uses unsteady RANS and applies the Shear Stress Transport (SST) turbulence model. The effect of tunnel length on both pressure and velocity fields is discussed. The variation of the pressure at the entrance and exit of the tunnel is also analysed and conclusions are drawn.

An improved transverse vibration techniques for enhancing heat transfer and temperature uniformity in viscous fluid flow

S. Tian, M. Barigou

School of Chemical Engineering, University of Birmingham, UK.

SXT200@bham.ac.uk

Abstract

Radial heat transfer in viscous pipe flow is controlled by thermal conduction which leads to a wide radial temperature distribution and slow heating of the core region of the flow. This is highly undesirable in many industrial processes as it results in a grossly uneven distribution of fluid heat treatment. The use of static in-line mixers to promote radial mixing and, thus, heat transfer and temperature uniformity, engenders large pressure drops and the devices are generally prohibited in processes where hygiene is paramount as they are difficult to keep clean. We recently reported a Computational Fluid Dynamics (CFD) study which showed that the superimposing of transverse mechanical oscillations on the steady flow of a viscous fluid in a pipe with an isothermal wall, results in a large enhancement in wall heat transfer as well as a considerably more uniform radial temperature distribution accompanied by rapid heating of the inner region of the flow. Such a transverse vibration also causes the thermal boundary layer to grow more rapidly and, thus, the temperature profile to develop very rapidly in the axial direction. In this paper, we report on an enhanced vibration technique which combines transverse oscillations with a step rotation of oscillation orientation. The improved performance of this new method is compared to that of the simple vibration technique reported in our previous work, as well as to the performance of the well-known Kenics helical static mixer.

Keywords: CFD; heat transfer enhancement; laminar flow; oscillations; temperature profile; vibration.

Single Driven Vortex Chain in a Confining Potential

Austin Tomlinson¹ and Nicola Wilkin¹

¹School of Physics and Astronomy, University of Birmingham, UK.

aat931@bham.ac.uk

We simulate artificial flow channels of superconducting vortex matter to study dynamical and non-equilibrium effects. The systems of interest are thin channels with regular arrays of edge vortices confining the free vortex motion. We study the “zig-zag” transition whereby a single flowing chain of vortices bifurcates into two flowing chains. The energetics and transitional time scales are examined, which are of interest to the community in this field [1,2]. BlueBEAR enables us to study a large parameter space in detail by running parallelised molecular dynamics simulations and analysis scripts.

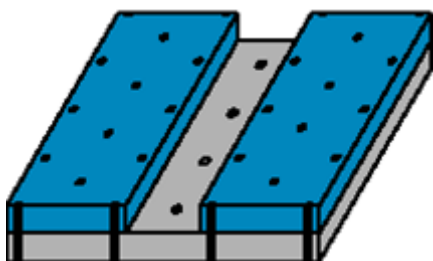


Figure 22: 3D perspective of the system. Two superconductors are layered together, with an etched channel in the top layer. Vortices pin into regular arrays on the top layer and can flow freely on the lower layer.

Figure 21: Top-down view of system. Units are scaled so that $a_0=1$.

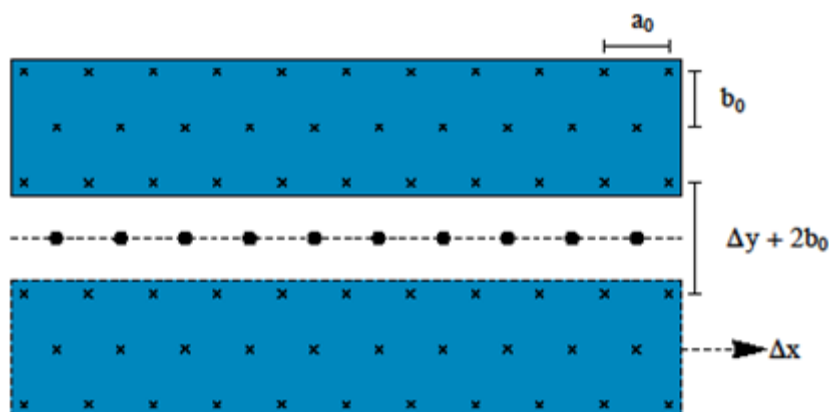


Figure 2 shows the general picture of the system [3]. Horizontal and vertical directions are denoted x and y , respectively. Pinned vortices are denoted by crosses, and free vortices by solid circles. The lattice parameters, a_0 and b_0 are related by $b_0 = a_0 \sqrt{3}/2$. The dashed line through the centre of the channel is defined to be $y = 0$. The channel width parameter, Δy , controls how the channel widens from commensurability. The channel offset parameter, Δx , controls the position of the entire lower channel edge. The channel is commensurate for $\Delta x = m\epsilon a_0$, where $m \in \mathbb{Z}$.

References

- [1] Delfau, J. B., Coste, C., & Saint Jean, M. 2013. Transverse single-file diffusion near the zig-zag transition. *Physical Review E*, **87**, 032163.
- [1] Piacenta, G., Schweigert, I. V., Betouras, J. J., & Peeters, F. M. 2004. Generic properties of a quasi-one-dimensional classical Wigner crystal. *Physical Review B*, **69**, 045324.
- [3] Besseling, R., Kes, P. H., Drose, T., & Vinokur, V. M. 2004. Depinning and dynamics of vortices confined in mesoscopic flow channels. *New Journal of Physics*, **7**(71).

Visualizing Synthetic Dental Biofilm on Teeth Using Dual Energy Micro Computed Tomography

N. Vyas¹, A. D. Walmsley², H. Dehghani³, E. Pecheva², L. Grover⁴, R.L. Sammons²

¹Physical Sciences of Imaging for Biomedical Sciences (PSIBS) Doctoral Training Centre, ²School of Dentistry, ³School of Computer Science, ⁴School of Chemical Engineering, University of Birmingham, UK

nxv264@bham.ac.uk

Dental calculus biofilms form naturally over time on tooth surfaces and dental implants. They can be removed using ultrasonic scalers in order to prevent periodontal diseases. It is therefore important to understand the different processes involved in removing dental biofilm to enable development of more efficient instrumentation. Imaging the disrupted biofilm can give insights into the removal process. For this reason, we investigated the possibility of using micro computed tomography (micro-CT) to image biofilms, initially by using an artificial biofilm hydrogel as a model system [1]. Dual energy imaging was done to overcome the contrast problem when simultaneously imaging

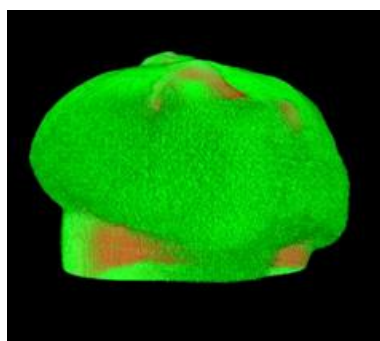


Figure 1: Micro-CT 3D reconstruction of artificial biofilm on a tooth after segmenting using dual energy analysis software. Hydrogel: green, tooth: red.

materials with high and low x-ray absorption coefficients.

We applied the hydrogel (stained with iodine) to the surface of a pre-molar tooth and imaged using micro-CT at low and high energies. The two scans were combined using dual energy analysis software, enabling effective segmentation of the hydrogel from the tooth. Noise reducing filters were applied to improve the segmentation. Accuracy of the dual energy segmentation was evaluated by comparing with a reference image and calculating sensitivity and specificity for different energy combinations. 99% sensitivity and specificity values were obtained with scans done at 30 kV and 70 kV, suggesting that dual energy imaging is an effective way to segment and analyse dental biofilm on a tooth.

This novel application of dual energy micro-CT will provide new insights into biofilm localisation after disruption, leading to further knowledge about how ultrasonic scalers remove dental biofilm. The methodology used can also be applied to other fields, such as imaging connective tissue interfaces [2].

References

- [1] R.G. Macedo, J.P. Robinson, B. Verhaagen, A.D. Walmsley, M. Versluis, P.R. Cooper & L.W.M. van der Sluis, "A novel methodology providing new insights into the ultrasonic removal of a biofilm-mimicking hydrogel from lateral morphological features of the root canal." *International Endodontic Journal*, 2014
- [2] A. Bannerman, J. Z. Paxton & L. M. Grover, "Imaging the hard/soft tissue interface" *Biotechnology letters*, 1-13, 2013